

1 **Peripheral microtubules ensure asymmetric furrow positioning in neural stem cells**

2

3 Running title: Peripheral microtubules not the spindle midzone, position the asymmetric  
4 division furrow in neural stem cells.

5

6 Alexandre Thomas<sup>1</sup>, Emmanuel Gallaud<sup>1</sup>, Aude Pascal<sup>1</sup>, Laurence Serre<sup>2</sup>, Isabelle Arnal<sup>2</sup>,  
7 Laurent Richard-Parpaillon<sup>1</sup>, Matthew Scott Savoian<sup>3</sup> and Régis Giet<sup>1#</sup>.

8

9 <sup>1</sup>. Univ Rennes, CNRS, IGDR (Institut de Génétique et Développement de Rennes) - UMR  
10 6290, F-35000 Rennes, France

11 <sup>2</sup>. Univ. Grenoble Alpes, Inserm U1216, CEA, CNRS, Grenoble Institut Neurosciences,  
12 GIN, 38000 Grenoble, France.

13 <sup>3</sup>. Massey University, School of Fundamental Sciences, 4410, Palmerston North, New  
14 Zealand

15

16 #. Corresponding author: [regis.giet@univ-rennes1.fr](mailto:regis.giet@univ-rennes1.fr)

17

18

19 **Abstract**

20 Neuroblast (NB) cell division is characterized by a basal positioning of the cleavage furrow  
21 resulting in a large difference in size between the future daughter cells. In animal cells, furrow  
22 placement and assembly is governed by centralspindlin, a highly conserved complex that  
23 accumulates at the equatorial cell cortex of the future cleavage site and at the spindle  
24 midzone. In contrast to model systems studied so far, these two centralspindlin populations  
25 are spatially and temporally separated in NBs. A cortical leading pool is located at the basal  
26 cleavage furrow site and a second pool accumulates at the midzone before travelling to the  
27 site of the basal cleavage furrow during cytokinesis completion. By manipulating microtubule  
28 (MT) dynamics, we show that the cortical centralspindlin population requires peripheral astral  
29 microtubules and the Chromosome Passenger Complex (CPC) for efficient recruitment. Loss  
30 of this pool does not prevent cytokinesis but enhances centralspindlin levels at the midzone  
31 leading to furrow repositioning towards the equator and decreased size asymmetry between  
32 daughter cells. Together these data reveal that the asymmetrical furrow placement  
33 characteristic of NBs results from a competition between spatially and functionally separate  
34 centralspindlin pools in which the cortical pool is dominant and requires peripheral astral  
35 microtubules.

36

## 37 **Introduction**

38

39 Cytokinesis in somatic cells ensures the equal partitioning of the segregated chromosomes  
40 and is responsible for the division of the mother cell's cytoplasm into two daughters. This  
41 process requires the highly orchestrated assembly and constriction of an acto-myosin  
42 contractile ring, usually at the cell's center. The use of various model systems has clearly  
43 established that the mitotic spindle defines the position of the contractile ring and the resulting  
44 cleavage furrow<sup>1,2</sup>. Two populations of mitotic spindle microtubules (MTs) have been shown  
45 to trigger the assembly of the contractile machinery during late anaphase. The first is a sub-  
46 population of astral MTs. These MTs emanate from the centrosomes to the equatorial cortex  
47 where they deliver furrow-inducing signals<sup>3-5</sup>. The second population, comprises the spindle  
48 midzone, a region of antiparallel MT overlap and interdigitation within the central spindle that  
49 assembles between the decondensing daughter nuclei. In many symmetrically dividing  
50 somatic cell types the relative contribution of these two populations has been difficult to  
51 unambiguously determine due to their close proximity at the cell's equator. Yet, experiments  
52 during the last few decades have helped to propose a common mechanism across model  
53 systems in which the furrow-inducing signals emanate from both cortical proximal astral MTs  
54 and the spindle midzone with each acting in parallel. However, these pathways do not appear  
55 to be equivalent. For instance, if the furrow is located away from the midzone, it will regress  
56 and a new one will be established at the midzone location<sup>1, 3, 6, 7</sup>. Thus, in equatorially  
57 dividing cells, the spindle midzone pathway acts dominantly and can reset furrowing.

58 Centralspindlin is the main orchestrator of furrowing. This protein complex is a tetramer  
59 composed of two subunits of the Kinesin 6 (Pavarotti-klp in *Drosophila melanogaster*) and  
60 two subunits of the MgcRacGAP (Tumbleweed in *Drosophila melanogaster*). Tumbleweed is  
61 essential for the activation of the Rho-GEF Ect2 (Pebble in *Drosophila melanogaster*). The  
62 formation of Rho-GTP triggers the local activation of Rho Kinase and phosphorylation of  
63 non-muscle Myosin Regulatory Light Chain, an event that stimulates myosin activation and  
64 ultimately drives cytoplasmic cleavage<sup>8,9</sup>. While it is well established that centralspindlin  
65 acts along central spindle MTs and accumulates at the cell cortex equator to promote  
66 symmetrical cleavage, far less is known about how this complex governs asymmetrical  
67 divisions. *Drosophila* neural stem cells (Neuroblasts, NBs) are characterized by a biased  
68 furrow placement towards the basal region of the cell. Asymmetric cytokinesis triggers the  
69 formation of a large apically positioned cell that retains the NB identity, and a small basal  
70 ganglion mother cell (GMC) that will undergo differentiation<sup>10</sup>. Asymmetry is apparent prior

71 to furrow initiation and can be detected during early anaphase as myosin redistributes from  
72 around the cortex to a more basal position <sup>11</sup>. Previous studies have shown that this process is  
73 under the strict control of the NB polarity machinery but is also influenced by the spindle  
74 midzone and the Chromosome Passenger Complex (CPC) <sup>12, 13</sup>. To better understand the  
75 mechanism of furrow positioning in asymmetrical cytokinesis, we have genetically  
76 manipulated spindle size and MTs dynamics in *Drosophila* NBs. Our data indicate that the  
77 mechanisms dictating asymmetrical daughter cell size are extremely robust and tolerate  
78 increases in spindle length and shape. We report that furrowing initiates away from the  
79 midzone, in a basal position through the action of a subcortical centralspindlin pool targeted  
80 by peripheral astral microtubules. When these MTs are ablated, centralspindlin recruitment at  
81 the furrow is impaired and becomes abnormally enriched at the midzone causing  
82 repositioning of the cleavage site, thus affecting the size asymmetry of the daughter cells.  
83 Together these results reveal that unlike most systems, in *Drosophila* NBs that are  
84 characterized by a high level of cell size asymmetry during cell division, a population of  
85 peripheral astral MTs, and not the spindle midzone, defines and maintains asymmetric  
86 cleavage furrow positioning.  
87

## 88 **Material and methods**

89

## 90 **Molecular biology**

91 Msps cDNA was provided by G. Rogers (University of Arizona, USA), amplified by PCR  
92 and inserted into pENTR (Life Technologies) to generate the pENTR-Msps entry clone.  
93 pENTR-Ensc has been previously described<sup>14</sup>. The pENTR-Feo and the pENTR-Tum entry  
94 clones were obtained from P.P D'Avino (University of Cambridge, UK). The pENTR-Feo  
95 and pENTR-Msps entry clones were each subsequently recombined into pTWV and pTWR  
96 (Carnegie Institute, USA) to generate constructs allowing the expression of Feo-VenusFP and  
97 Msps-RFP fusion proteins, respectively, under the control of the GAL4 protein using the  
98 Gateway recombination cloning technology (Life Technologies). pENTR-Ensc was  
99 recombined into pDEST-MBP (a gift from H. Ohkura, University of Edinburgh, UK) to allow  
100 the expression of a recombinant Ensconsin protein with a C-terminal MBP tag.

101

## 102 **Fly stocks**

103 All flies were maintained under standard conditions at 25°C. The *ensconsin* mutant fly stocks  
104 *enscAnull* and *enscΔN*, referred to *ensc* flies, were characterized previously (Sung et al 2008).  
105 UAS-Ensconsin-Venus transgenic flies, overexpressing Ensconsin-Venus, have been  
106 described<sup>15</sup>. UAS-Feo-Venus and UAS-Msps-RFP overexpressing flies were obtained from  
107 BestGene (USA) following P-element mediated transformation. UAS-Klp10A flies were  
108 supplied by C. Dahmann (Max Planck Institute, Germany)<sup>16</sup>. UAS-Klp67A (ID # F001232)  
109 stock was obtained from FlyORF<sup>17</sup>. UAS-Klp67A-RNAi (VDRC ID 52105) and UAS-Mad2-  
110 RNAi (VDRC ID 106003) transgenic fly lines were obtained from the Vienna Drosophila  
111 RNAi Center<sup>18</sup>. Sqh-GFP<sup>19</sup>, UAS-GFP-Pav-klp and Ubiquitin-βtub-GFP expressing flies<sup>20</sup>,  
112<sup>21</sup> were supplied by R. Karess (Institut Jacques Monod, France) and by D. Glover (University  
113 of Cambridge, UK), respectively. The Pavarotti mutant *pav<sup>B200</sup>* flies were obtained from E.  
114 Montembault (Institut Europeen de Chimie et Biologie, France)<sup>22</sup> and Survivin mutant allele  
115 *svn<sup>2180</sup>* flies were courtesy of Jean-René Hyunh (College de France, France)<sup>23</sup>. Flies  
116 expressing the membrane-localized PH-PLCδ-GFP and PH-PLCδ-RFP proteins were  
117 provided by A. Guichet (Institut Jacques Monod, France)<sup>24, 25</sup>. RFP-Tubulin flies were  
118 provided by R. Basto (Institut Currie, France). The GFP-AurA expressing fly stock was  
119 described previously<sup>26</sup>. The following stocks were obtained from the Bloomington Stock  
120 Center: Feo-GFP expressed under the ubiquitin promoter (BDSC 59273,<sup>27</sup>), *sas-4<sup>s2214</sup>* mutant

121 (BDSC 12119, <sup>28</sup>), 69B-Gal4 (BDSC 1774), Insc-Gal4 (BDSC 8751), UAS-mCherry- $\alpha$ -  
122 tubulin (BDSC 25774 and BDSC 25773). The 69B-Gal4 fly stock was used to drive over-  
123 expression in the fly CNS for the following UAS regulated transgenes: Ensconsin, Klp67A,  
124 Msps, GFP-Pav-Klp together with *Mad2* RNAi and UAS-mCherry. The Insc-Gal4 strain was  
125 used to drive over-expression of Ensconsin, Klp10A, UAS- GFP-Pav-klp, Feo-Venus and  
126 mCherry- $\alpha$  tubulin transgenes in the central brain.

127

### 128 **Production of recombinant proteins**

129 MBP and Ensconsin-MBP were induced in *E.coli*, for 4 h at 25°C. The proteins were purified  
130 on amylose column as described by the manufacturer (BioLabs) and stored in small aliquots  
131 at -80°C.

132

### 133 **TIRF microscopy and analysis of MT dynamics**

134 Tubulin was purified from bovine brain and fluorescently labeled with ATTO 488 and ATTO  
135 565 or biotinylated as described before <sup>29,30</sup>. Briefly, microtubule seeds were prepared from  
136 biotinylated and ATTO-565-labeled tubulin in the presence of Guanosine-5'-[( $\alpha,\beta$ )-  
137 methyleno]triphosphate (GMPCPP) in BRB80 buffer (80 mM Pipes, 1 mM EGTA, 1 mM  
138 MgCl<sub>2</sub>, pH 6.74) <sup>30</sup>. Flow chambers were prepared with functionalized silane-PEG-biotin  
139 coverslips and silane-PEG glass slides, as previously described (Ramirez-Rios et al., 2017).  
140 The chamber was successively perfused at room temperature with neutravidin (25  $\mu$ g/ml in  
141 1% BSA in BRB80), PLL-g-PEG (2 kD, 0.1 mg/ml in 10 mM Hepes, pH 7.4), BSA (1% in  
142 BRB80 buffer) and microtubule seeds. The following assembly mixture was then injected: 14  
143  $\mu$ M tubulin (containing 15 % ATTO-488-labeled tubulin) without or with 200 nM MBP or  
144 MBP-Ensconsin in TIRF assay buffer (4 nM DTT, 50 mM KCl, 1% BSA, 1 mg/mL glucose,  
145 70  $\mu$ g/mL catalase, 580  $\mu$ g/mL glucose oxidase, 0.05% methylcellulose (4000 centipoise) in  
146 BRB80). Time-lapse images were recorded at 35°C at a rate of one frame per 5 seconds on an  
147 inverted Eclipse Ti Nikon microscope equipped with an Apochromat 60X1.49 N.A oil  
148 immersion objective, an iLas<sup>2</sup> TIRF system (Roper Scientific), and a cooled charge-coupled  
149 device camera (EMCCD Evolve 512, Photometrics) controlled by MetaMorph 7.7.5 software.  
150 Microtubule dynamic parameters were analyzed in Image J on kymographs obtained using an  
151 in-house KymoTool macro (available upon request to eric.denarier@univ-grenoble-alpes.fr).  
152 Growth and shrinkage rates were determined from the slopes of microtubule growth and  
153 shrinkage phases. The catastrophe and rescue frequencies were calculated by dividing the

154 number of events per microtubule by the time spent in growing and shrinking states,  
155 respectively.

156

### 157 **Antibodies and Western blotting**

158 The following antibodies and concentrations were used in this study: polyclonal rabbit anti-  
159 Msps (1:5000) provided by J. Raff <sup>31</sup>, polyclonal rabbit anti-Klp67A (1:500) supplied by G.  
160 Goshima <sup>32</sup>, polyclonal rabbit anti-Klp10A (1:1000) was courtesy of G. Rogers <sup>33</sup> and rabbit  
161 anti-Myosin (1:2000) was provided by R. Karess <sup>34</sup>. The anti-Enscosin antibody raised  
162 against the Kinesin binding domain has been previously described<sup>14</sup>. Rabbit anti-PKC $\zeta$  (C-20,  
163 1:200) and anti-actin polyclonal antibodies (sc-1616, 1:5000) were obtained from Santa Cruz  
164 Technology. Monoclonal mouse anti-alpha Tubulin (clone DM1A, T2199; 1:500) and rabbit  
165 polyclonal anti-phosphorylated histone H3 (Ser10) (06570, 1:500) antibodies were obtained  
166 from Millipore. Monoclonal rat anti-Miranda antibody (ab197788, 1:1000) was obtained from  
167 Abcam. Secondary antibodies were labelled with either Alexa Fluor-conjugated (1:1000) or  
168 peroxidase-conjugated secondary antibodies (1:5000), each obtained from Life Technologies.  
169 For Western Blotting ECL reagents were purchased from ThermoFisher.

170

### 171 **Live cell microscopy**

172 Third-instar larval brains were dissected in Schneider's *Drosophila* medium supplemented  
173 with 10% FCS. Isolated brains were loaded and mounted on stainless steel slides, and the  
174 preparations were sealed with mineral oil (Sigma-Aldrich) as previously described <sup>14</sup>. For MT  
175 depolymerization experiments, larval brains were incubated during 30 min in the above  
176 medium supplemented with colchicine at a final concentration of 15  $\mu$ M. After incubation,  
177 brains were mounted and processed for live cell imaging.

178 Images were acquired at 25°C using a CSU-X1 spinning-disk system mounted on an inverted  
179 microscope (Elipse Ti; Nikon) equipped with a 60X 1.4 NA objective. At 20, 30 or 60 sec  
180 intervals 10 z-steps were acquired with 1 $\mu$ m intervals. Fluorescent protein probes were  
181 excited with 488nm or 561nm laser light and the images were captured using a sCMOS  
182 ORCA-Flash4.0 (Hamamatsu) camera. Recordings were controlled using MetaMorph  
183 acquisition software. Data were processed in ImageJ and viewed as maximum-intensity  
184 projections prior to analysis or figure preparation.

185

### 186 **Photo-ablation experiments**

187 Photo-ablations were performed with a Mai-Tai two-photon infrared laser (Spectra Physics)  
188 attached to a Leica SP5 confocal microscope equipped with a 60X 1.3 NA objective with the  
189 stage maintained at 25°C. Z-series consisting of 10, 1µm steps were acquired before and after  
190 the photo-ablation at 30 sec intervals. Photo-ablation was performed on the basal centrosome  
191 using flies expressing GFP-H2A, PH-PLCδ-GFP and Aurora A-GFP. Anaphase onset was  
192 identified as the first signs of sister chromatid separation. The photo-ablation was considered  
193 complete after the Aurora A signal on the basal centrosome could no longer be detected.

194

### 195 **Live cell imaging analysis**

196 Measurements of fluorescence intensities, mitotic spindle lengths and diameters of NB and  
197 GMC cells were performed with ImageJ software<sup>35</sup>. The Sqh-GFP analyses were done on the  
198 maximum projection of two optical sections (1 µm). The polarity-dependent apical clearing  
199 was calculated, as the first time point after anaphase onset, when myosin began to disappear  
200 from the apical cortex<sup>36</sup>. NB cortex curvature analyses were performed according to  
201 previously defined methods<sup>13</sup>. The furrow shift was determined as the distance between the  
202 first ingression site and final cleavage site. To quantify the Myosin-GFP furrows width; a  
203 segmented line was drawn along the NB half-cell cortex during anaphase and the GFP  
204 intensity profiles were quantified along this line using ImageJ. The furrow width was  
205 measured as the relative half-cell cortex length containing 60% of the maximum Sqh-GFP  
206 signal intensity.

207

### 208 **Immunofluorescence analysis**

209 Larval brains from each genotype were processed for immunofluorescence studies as  
210 described previously<sup>14</sup>. Briefly, wandering third instar larval brains from were dissected in  
211 testis buffer (TB: 183 mM KCL, 47 mM NaCl, 10 MM Tris, and 1 mM EDTA, pH 6.8) and  
212 brains were fixed for 20 minutes at 25°C in TBF (TB supplemented with 10% formaldehyde,  
213 and 0.01% Triton X-100). Brains were then washed twice in PBS for 15 minutes, and twice in  
214 PBS Triton X-100 0.1% for 15 minutes. The brains were first incubated for 60 minutes at  
215 25°C in PBSTB (1% BSA), before incubation with secondary antibodies. The samples were  
216 observed with a SP5 confocal microscope (Leica) equipped with a 63X 1.4 NA objective lens.  
217 Images are maximum intensity projections consisting of 4 optical sections acquired at 0.5 µm  
218 intervals.

219

220 **Quantification of peripheral MTs in fixed NBs during mid anaphase**

221 Z-series were acquired every 0.2  $\mu\text{m}$  using a LSM 880 confocal microscope with Airyscan  
222 (Zeiss) for telophase NBs. Images were then processed with the Zen software. Images were  
223 analyzed with ImageJ as maximum intensity projections (0.8  $\mu\text{m}$ ) consisting of 5 optical (0.2  
224  $\mu\text{m}$ ) sections in the plane of the furrow.

225

226 **Statistical analysis**

227 Differences between datasets were assessed with Prism 7.0a software (GraphPad), either by  
228 non-parametric tests (Mann-Whitney-Wilcoxon) or parametric tests (Unpaired T). Non-  
229 significance (ns) threshold was when  $P > 0.05$ .

230

231

232

233

234

235

236

237



238 **Results**

239

240 **Cell size asymmetry is compromised following Ensconsin depletion but not over-**  
241 **expression in NBs**

242 Neuroblasts divide asymmetrically to generate a large self-renewing neuroblast (NB) and a  
243 smaller differentiating ganglion mother cell (GMC, Figure 1 A. We previously showed that  
244 Ensconsin is required for MT polymerization during cell division; consequently *ensc* mutant  
245 spindles are shorter than their wild type (WT) counterparts<sup>14</sup>. To investigate the possible  
246 consequences of a change in spindle length on NB asymmetric cell division, we first  
247 analyzed, by live cell imaging, cell size asymmetry of dividing NBs in wild type and *ensc*  
248 mutants (Figure 1). We confirmed the previous finding that loss of Ensconsin triggered a  
249 ~10% decrease in mitotic spindle length (Figure 1 B, C). Strikingly, the *ensc* mutants  
250 displayed a small yet statistically significant reduction in the ratio between NB and GMC  
251 diameters indicating a loss of asymmetry (Figure 1 D). This defect could either result from the  
252 associated change in spindle length or indicate some uncharacterized function for Ensconsin  
253 in asymmetrical size fate determination. To further explore the role of Ensconsin in MT  
254 dynamics *in vitro*, we used TIRF microscopy and recombinant Ensconsin protein (Figure 1  
255 E). Ensconsin-MBP had a small but significant effect on MT growth rate. Most striking was  
256 the ~50% reduction in the rate of MT shrinkage and the more than 3 times increase in the  
257 rescue frequency compared to controls or MBP alone (Figure 1 F). In line with these results,  
258 over-expression of Ensconsin (Ensc-OE) in NBs lead to elongated spindles that buckled when  
259 reaching the cortex (Figure 1 G, H, S1), consistent with previous work in symmetrically  
260 dividing S2 cells<sup>14</sup>. Despite the increase in MT polymerization and spindle length, the level  
261 of size asymmetry remained unperturbed following cytokinesis in Ensc-OE NBs (Figure 1 D).

262

263 **Enhancement of spindle length through over-expression of Msp8 or depletion of**  
264 **Kinesin-8 MT depolymerase does not alter cell size asymmetry**

265 To determine if daughter cell size asymmetry is insensitive to stimulation of MT growth, we  
266 quantified size asymmetry following over-expression of the microtubule associated protein  
267 Mini spindles, the fly orthologue of MAP215/ch-TOG, a protein with MT polymerization  
268 properties<sup>37-39</sup>. In parallel, we performed RNAi-mediated depletion of the MT  
269 depolymerizing Kinesin-8 fly family member Klp67A. This kinesin depolymerizes  
270 microtubules and its depletion leads to the formation of exceptionally long spindles in  
271 *Drosophila* cells<sup>40, 41</sup>. Similar to Ensc-OE, over-expression of Msp8-RFP (Msp8-OE) or

272 RNAi-mediated depletion of Klp67A led to the formation of long and bent mitotic spindles  
273 (Figure 2 A, B and D; Figure S1; Video 1 and 2). Neither perturbation affected the post-  
274 cleavage asymmetrical cell size (Figure 2A, C and E). These data suggest that asymmetric cell  
275 size regulation is not sensitive to an increase in MT polymer or spindle length elongation.

276

### 277 **Spindle shortening through over-expression of Kinesin-8 or -13 family MT** 278 **depolymerases decreases cell size asymmetry**

279 To investigate if the size asymmetry reduction observed in *ensc* mutants (Figure 1) was  
280 unique to Ensconsin or rather a common effect of spindle shortening, we induced other  
281 perturbations of MT-polymerization by over-expressing two MT depolymerizing kinesins;  
282 either Klp10A which belongs to the Kinesin-13 family (Klp10A-OE) or the Kinesin-8  
283 member Klp67A (Klp67A-OE) (Figure S1). Importantly, whereas the depletion of either  
284 causes spindle elongation, their over-expression results in abnormal shortening<sup>40, 42-45</sup>. As  
285 predicted both Klp10A-OE and Klp67A-OE NBs exhibited shorter spindles although the  
286 length reduction was more pronounced in Klp10A-OE cells (Figure 2 F, G, I Video 3).  
287 Depending on the spindle's length, it assumed a lesser or greater displacement relative to the  
288 cell center. Interestingly, in these shortened spindle cells, like with *ensc* mutants, we found  
289 that the NB/GMC diameter ratio was significantly impaired indicating that cell division was  
290 more symmetric compared to controls (Figure 2 H and J). Thus, defective MT polymerization  
291 leading to spindle shortening due to loss of Ensconsin function or over-expression of the  
292 Kinesin- 8s and 13s biases asymmetric cell division.

293

### 294 **Defective MT growth leads to an apical shift of the basal cleavage furrow after anaphase** 295 **onset.**

296 In asymmetrically dividing NBs, it was described that both polarity and midzone-dependent  
297 mechanisms ensure that furrow components, including myosin, are positioned basally to  
298 generate daughter cells of different sizes<sup>11, 13, 36</sup>. To investigate the behavior of the furrow, we  
299 monitored the dynamics of the regulatory light chain of myosin in live NBs using Sqh-GFP<sup>46</sup>.  
300 In control cells, we confirmed that Myosin-GFP was uniformly present at the cell cortex  
301 before anaphase (Figure 3 A and Video 4). In *ensc*, Klp67A-OE and Klp10A-OE NBs, the  
302 polarity-dependent step of myosin redistribution from the apical cortex was similar to  
303 controls, in agreement with the perturbations not altering cell polarization (Figure S2 A and  
304 B). We also analyzed the furrow positioning through curvature measurements of the cell  
305 membrane (<sup>13</sup> and Figure 3 B). While the furrow position remained stably placed from

306 anaphase until cytokinesis in control NBs, we found it shifted significantly towards the apical  
307 side during completion of cell division in *ensc* and Klp67A-OE cells, with a maximal  
308 displacement observed for Klp10A-OE NBs (Figure 3, C Video 5 and 6). Moreover, while the  
309 furrow width was consistently ~10% of the half-cell cortex length in control NBs as revealed  
310 by Myosin-GFP (Figure 3 D and E), the signal occupied a larger space in *ensc* and Klp67A-  
311 OE NBs with the maximum width of ~25% of the half-cell cortex length observed for  
312 Klp10A-OE cells at comparable time points (Figure 3 A, E, Video 6). From this we conclude  
313 that proper MT growth is required for maintaining furrow size and position during  
314 asymmetrical cell division.

315

### 316 **Centralspindlin is spatially and temporally regulated as two distinct populations**

317 Our previous perturbations, which interfered with MT dynamics, suggested that a common  
318 mechanism was at play for maintaining the furrow position. In all higher eukaryotes examined  
319 to date, myosin recruitment and activation at the cleavage furrow is regulated by the highly  
320 conserved centralspindlin complex, a tetramer comprised of a Kinesin-6 family member  
321 complexed with Mgc-RacGAP (Pavarotti-klp and Tumbleweed in *Drosophila*, respectively)<sup>7</sup>,  
322 <sup>8,47</sup>. Strikingly, we found that the combination of Klp10A-OE and a single copy of the *pav*<sup>B200</sup>  
323 null allele enhanced the asymmetry defect observed with Klp10A-OE alone (Figure S2 C).  
324 Centralspindlin functionality and targeting to the membranes is regulated by the chromosomal  
325 passenger complex (CPC)-dependent oligomerization<sup>48</sup>. We therefore challenged the  
326 complex by introducing a single null allele for its Survivin subunit, *svn*<sup>2180</sup>, and monitored the  
327 effects on cell symmetry in the Klp10A-OE background. We found that Klp10A-OE-  
328 dependent size asymmetry defects were further enhanced when Survivin levels were reduced  
329 (Figure S2 C). These results suggest that the observed asymmetry defects are due, at least in  
330 part, to impaired centralspindlin function.

331 In most eukaryotic cells, the centralspindlin complex is located at the spindle midzone and at  
332 the equatorial cortex. To characterize the furrow mis-positioning that accompanies defective  
333 microtubule growth, we analyzed the spatio-temporal distribution of the motor component of  
334 centralspindlin, Pavarotti-klp, in different experimental backgrounds. We began by examining  
335 GFP-Pav-klp<sup>21</sup> localization in control NBs. Our time-lapse studies showed that most of the  
336 GFP-Pav-klp was located at the cortex at the cleavage site. Following the onset of furrow  
337 ingression, a second pool started to accumulate into a small and spatially distinct band near  
338 the former site occupied by the metaphase chromosomes at the spindle midzone (Figure 4 A,  
339 Figure S3A, and Video 7). The spatial and temporal separation of the GFP-Pav-klp signals led

340 us to speculate that these were separate pools of centralspindlin. To confirm this hypothesis,  
341 we tracked GFP-Pav-klp in cells lacking MTs that were forced into anaphase using *Mad2*  
342 RNAi to abrogate the spindle assembly checkpoint<sup>14</sup>. Under these conditions GFP-Pav-klp  
343 showed a slight enrichment at the basal cortex but this pool remained at almost baseline levels  
344 compared to control cells, which showed continuous recruitment of GFP-Pav-klp following  
345 anaphase onset (Figure S3 B and C). When microtubule polymerization was impaired in *ensc*,  
346 Klp10A-OE and Klp67A-OE cells, even if the centralspindlin component GFP-Pav-klp was  
347 initially present at the equatorial cell cortex, it did not become enriched at the cleavage site to  
348 the levels measured in controls (Figure 4 B, C, E red triangles, Figure S4 A, see also Video 8  
349 and 9). Instead, in Klp10A-OE (Video 9), Klp67A-OE but not in *ensc* NBs (Video 8), GFP-  
350 Pav-klp appeared more abundant at the spindle midzone (Figure 4 B and C, see time 100 s  
351 blue arrows and insets at time 180 sec, Figure 4 E and Figure S4 B). Together, these  
352 experiments show that centralspindlin exists as two distinct and separable populations, one at  
353 the basal cortex and one at the spindle midzone. The decrease of the cortical centralspindlin  
354 pool is always accompanied by a displacement of the cleavage furrow.

355

### 356 **The spatio-temporal regulation of centralspindlin relies on stable peripheral MTs**

357 Fluorescence quantification (Figure 4 F) revealed that compared to wild type, Klp10-OE and  
358 Klp67A-OE NBs both displayed a decrease in cortical GFP-Pav-klp signal with a concomitant  
359 increase at the midzone (Figure S4). To further characterize the relationship between cortical  
360 and midzone centralspindlin pools and the role of MT growth in asymmetrical cleavage, we  
361 examined GFP-Pav-klp dynamics in *sas4<sup>s2214</sup>* mutants, which lack centrosomes and their  
362 associated astral MTs<sup>28</sup>. In this background, cortical enrichment also appeared diminished  
363 relative to the midzone (Figure 4 D, Figure S4 A and B). An enlarged view of the boxed  
364 regions for 180 sec post-anaphase onset highlights this increased centralspindlin recruitment  
365 at the spindle midzone and weaker accumulation at the cell cortex (Figure 4 E). Although  
366 *sas4<sup>s2214</sup>* NBs exhibited signal enrichment at their midzones, not all cells had a clear cortical  
367 reduction (Figure S4). Strikingly, *sas4<sup>s2214</sup>* mutants exhibited both an increased spindle length  
368 as well as a significant overall cell size asymmetry defect (Figure S5 A and B), further  
369 supporting the idea that astral MTs maintain basal furrow position. To confirm the  
370 contribution of the MT-aster in furrow positioning and maintenance, we removed it by laser  
371 ablation of the basal centrosome. Each centrosome was labeled with GFP-tagged Aurora A  
372 and basal proximal centrosome was ablated by a multi-photon laser until the signal was no  
373 longer detectable. Consistent with centrosome removal, ablated cells displayed a phenotype

374 virtually identical to *sas4*<sup>s2214</sup> mutants: daughter cells exhibiting cell size asymmetry after the  
375 ensuing cytokinesis (Figure S5 C and D, Video 10, compare left and right). These live cell  
376 observations suggested that astral MTs were essential to furrow positioning. We therefore  
377 performed a quantitative analysis of fixed preparations examining MT distribution during  
378 early telophase. Detailed morphological examination revealed that in wild type NBs bundles  
379 of astral MTs capped the future ganglion mother cell and spread apically, closely apposed to  
380 the cortex at the cleavage furrow. This was not the case with *ensc*, Klp67A-OE or Klp10-OE  
381 NBs, which showed decreased MT densities and lacked the presumptive bundles (Figure S5 E  
382 and F). Altogether, our data strongly suggest that peripheral astral MTs originating from the  
383 basal centrosome, in a close vicinity of the basal furrow play a key role in accurate  
384 asymmetric cell division.

385

### 386 **The early spindle midzone and furrow occupy distinct positions in NBs**

387 The presence of GFP-Pav-klp at the spindle midzone distal to the cleavage site and the  
388 movement of the furrow towards the equator in peripheral MTs-deficient cells prompted us to  
389 further characterize the cleavage site and the midzone in wild type cells. For this purpose, we  
390 used Fascetto-GFP (the homologue of the mammalian PRC1 protein; Feo-GFP) a marker that  
391 uniquely labels the spindle midzone (Figure 5 A)<sup>27, 49</sup>. We found that in these NBs the  
392 metaphase plate was slightly shifted toward the basal side relative to the cell equator along the  
393 apico-basal axis (Figure 5 A, -120 sec, arrowhead and Figure 5 C) but similarly placed to the  
394 midzone-defining Feo-GFP signal that appears following anaphase chromosome segregation  
395 (Figure 5 A, time 90 sec, and Figure 5 D arrowhead). This was in contrast to the position of  
396 the furrow (Figure 5 A, time 90, compare green and white arrows; E arrowhead). Indeed,  
397 while the metaphase plate and midzone were interchangeably located, the furrow was always  
398 distinct and basally distal to these (Figure 5 F, Video 11). Interestingly, kymograph analyses  
399 of the spindle midzone and cell membranes reveals that the midzone moves basally during the  
400 ingression of the furrow until they ultimately consolidate into a single structure (Figure 5 B).  
401 In summary, these data demonstrate that the spindle midzone in wild type cells occupies a  
402 spatially different position than that of the furrow and its associated cortical MTs. Both of  
403 these can recruit centralspindlin, however, under normal circumstances it is the cortical pool  
404 that dominates in *Drosophila* NBs to define the cleavage site.

## 405 **Discussion**

406

407 Asymmetric cell division is a robust process that ensures that two daughter cells inherit  
408 different fates and sizes. The *Drosophila* NB is a powerful and widely used model system to  
409 study this specialized form of division because of the large number of NBs in the developing  
410 *Drosophila* brain, rapid division time and experimental traceability<sup>50-52</sup>. Moreover, although  
411 these cells are relatively small, they are highly asymmetrical following cytokinesis allowing  
412 accurate measurements and analyses. In this study, we have used this model system to  
413 challenge asymmetric cell division after modification of MT growth dynamics. We were able  
414 to increase mitotic spindle length using over-expression of MT polymerizing MAPs (Msp  
415 and Ensconsin), as well as by RNAi-mediated depletion of Klp67A, a member belonging to  
416 Kinesin-8 family of MT depolymerizing Kinesins. Despite the presence of long and bent  
417 mitotic spindles under these conditions, the NB cell size ratio remained unchanged relative to  
418 wild type NBs. This reveals that asymmetric cell division and asymmetric positioning of the  
419 cleavage furrow are resistant to an excess of abnormally long and stable MTs during cell  
420 division. By contrast, decreasing MT stability and shortening of the mitotic spindle produced  
421 more symmetric cell divisions. This change was due to an apical shift of the cleavage furrow  
422 during its ingression. This phenotype was not MAP specific since over-expression of either  
423 Klp10A (Kinesin-13) or Klp67A (Kinesin-8) MT depolymerases, as well as the deletion of  
424 *Ensconsin* produced similar effects. Rather they suggest that spindle size or interference with  
425 microtubule dynamics is responsible for the phenotype. Interestingly, *sas-4*<sup>s2214</sup> mutants  
426 which are reported to lack functional centrosomes and thus astral microtubules yielded  
427 reduced levels of cell size asymmetry although these NBs harbored longer mitotic spindles<sup>28</sup>.  
428 This reveals that astral MTs and not the mitotic spindle length is the key element responsible  
429 for the level of size asymmetry observed in NBs. Consistent with this hypothesis, loss of the  
430 basal MT-aster, through targeted laser irradiation and ablation prior anaphase onset, also  
431 reduced sibling cell size asymmetry. Taken together these results strongly suggest that a  
432 population of basal peripheral astral MTs is required to maintain a cleavage site, which  
433 normally favors a basal position in the fly neuroblast. In agreement with this our  
434 quantification of peripheral MT bundles close to the ingression furrow revealed that they are  
435 significantly decreased during telophase in *ensc*, Klp10A-OE and Klp67A-OE NBs. Our  
436 results are in accord with reports indicating that a subpopulation of stable astral MTs play a  
437 key role in the initiation of furrowing in symmetrically dividing cells and that in some  
438 systems, furrowing can occur without the presence of a stable central spindle<sup>3, 6, 7, 20, 53-56</sup>.



439 However in contrast to other studies which utilize micromanipulation and laser ablation, our  
440 data reveals that in wild type asymmetrically dividing NBs, the astral MT furrowing pathway  
441 dominates over the midzone pathway. Previous studies have suggested that NBs have two  
442 genetically separable pathways to drive cytokinesis. The first, cortical polarity pathway, is  
443 responsible for the targeting of the furrowing machinery to the basal cortex on the surface of  
444 what is destined to become the smaller differentiating ganglion mother cell<sup>11,12</sup>. Interference  
445 with this polarity pathway prevents myosin enrichment at the basal cortex, leading to  
446 symmetric division. The alternative spindle pathway relies on the spindle midzone and the  
447 chromosomal passenger complex<sup>9,12</sup>. However, several of our observations are at odds with  
448 these previous findings and favor a model of furrow positioning that relies largely on  
449 peripheral astral MTs with little if any contribution from the spindle midzone; (i) live cell  
450 imaging and analyses utilizing GFP-Pav-klp as a marker of centralspindlin position revealed  
451 that this master controller of cytokinesis accumulated at the basal cortex throughout the entire  
452 furrow ingression process. (ii) Centralspindlin levels were low at the midzone during furrow  
453 placement and ingression compared to the cortex (Figure 4). (iii) We consistently observed  
454 that the midzone, as defined independently using both GFP-Pav-klp and Feo-GFP, was  
455 spatially independent from the furrowing site (Figures 5B, 6A). In addition, the midzone  
456 ultimately moved to the position of the furrow and not vice-versa (Figure 5B), confirming  
457 previous observations in embryonic NBs<sup>57</sup>. (iv) Finally, genetic or photo-based removal of  
458 the basal centrosome precluded peripheral MT formation and interaction with the cortex.  
459 Accordingly, the cortical centralspindlin pool was diminished and cells experienced a size  
460 asymmetry defect (Figure 4 and S4).

461 Our localization studies employing Feo-GFP suggest that under normal conditions midzone-  
462 associated centralspindlin does not perform a key role in positioning of the cleavage site and  
463 that this function is served by the more abundant centralspindlin pool associated with the  
464 membranes at the cleavage site. However, when peripheral MTs were impaired,  
465 centralspindlin enrichment at the furrow was diminished, leading to a decreased  
466 midzone/furrow centralspindlin ratio and a reset of the furrowing toward the equatorial  
467 midzone. This indicates that the two populations of centralspindlin are competent to signal  
468 furrowing but that the cortical pool delivered by astral MTs is normally dominant. Thus the  
469 spatial localization and the cortical/midzone ratio of centralspindlin are the pivotal  
470 determinants of final furrow positioning in the *Drosophila* NB. Interestingly, a recent study  
471 has shown that a similar competition between centralspindlin pools also occurs in human cells  
472<sup>58</sup>, revealing an evolutionary conservation of the mechanism.

473 As with human cells, we found that the CPC activity seems essential in this regulatory event  
474 (Figure S2 C). In contrast to a recent study in S2 cells, we do not observe GFP-Pav-klp  
475 labelling at the plus ends of astral MTs<sup>59</sup> even when studied by enhanced resolution imaging  
476 methods. Instead, we consistently find that centralspindlin coats the entire length of astral  
477 MTs, suggesting that the plus end directed motor activity of Pav-klp is used to bring  
478 centralspindlin to the furrow in *Drosophila* NBs in agreement with previous studies in early  
479 embryos<sup>21, 60</sup>.

480 Altogether, our data suggest a model in which a competition between different centralspindlin  
481 populations is a key determinant of asymmetric division in *Drosophila* NBs. The concerted  
482 and consecutive action of polarity cues and astral MTs as centralspindlin delivery arrays are  
483 essential in this process. The ability of the spindle midzone to define furrow and cleavage  
484 location only becomes engaged during late telophase and after subcortical astral MTs are  
485 compromised. Despite their clear role in governing size asymmetry, we have not been able to  
486 induce complete daughter cell size equality through any of a host of MT perturbing  
487 treatments. This suggests that additional feedback mechanisms exist to ensure a threshold  
488 level of asymmetry in these cells. Elucidating these systems and their evolutionary advantages  
489 will be important directions for future investigations.

490



491 **Acknowledgments**

492

493 We thank Gregory Rogers, Pier Paolo d'Avino, Renata Basto, Gohta Goshima, Jordan Raff,  
494 Hiro Ohkura, Anne Royou, Roger Karess, Christian Dahmann, Antoine Guichet, Juliette  
495 Mathieu, Jean-René Huynh, Clemens Cabernard, Tri Pham for providing fly stocks,  
496 antibodies and cDNAs. We thank Chloé Rauzier for preliminary functional analyzes of Ensc-  
497 OE and Msps-OE NBs. This work was funded by the Ligue Nationale Contre le Cancer, the  
498 Fondation ARC pour la Recherche sur le Cancer. A. T. is a doctoral fellow of the Région  
499 Bretagne and the Ligue Nationale contre le Cancer. We thank the Photonic Imaging Center of  
500 Grenoble Institute of Neurosciences, which is part of ISdV core facility. We thank Xavier  
501 Pinson, Stéphanie Dutertre and Sébastien Huet for advices and help with the microscopes and  
502 the Microscopy Rennes Imaging Center platform. We thank Romain Gibeaux, Pier Paolo  
503 d'Avino and Christelle Benaud for ideas, critical readings and helpful suggestions. The  
504 authors have no competing financial interests to declare.

505 **References**

506

- 507 1. von Dassow, G. Concurrent cues for cytokinetic furrow induction in animal cells.  
508 *Trends Cell Biol* **19**, 165-173 (2009).
- 509 2. Rappaport, R. Cytokinesis in animal cells. *Int Rev Cytol* **31**, 169-213 (1971).
- 510 3. Foe, V.E. & von Dassow, G. Stable and dynamic microtubules coordinately shape the  
511 myosin activation zone during cytokinetic furrow formation. *J Cell Biol* **183**, 457-470  
512 (2008).
- 513 4. Vale, R.D., Spudich, J.A. & Griffis, E.R. Dynamics of myosin, microtubules, and  
514 Kinesin-6 at the cortex during cytokinesis in *Drosophila* S2 cells. *J Cell Biol* **186**, 727-  
515 738 (2009).
- 516 5. Shannon, K.B., Canman, J.C., Ben Moree, C., Tirnauer, J.S. & Salmon, E.D. Taxol-  
517 stabilized microtubules can position the cytokinetic furrow in mammalian cells. *Mol*  
518 *Biol Cell* **16**, 4423-4436 (2005).
- 519 6. Bringmann, H. & Hyman, A.A. A cytokinesis furrow is positioned by two consecutive  
520 signals. *Nature* **436**, 731-734 (2005).
- 521 7. Mishima, M. Centralspindlin in Rappaport's cleavage signaling. *Seminars in cell &*  
522 *developmental biology* **53**, 45-56 (2016).
- 523 8. D'Avino, P.P., Giansanti, M.G. & Petronczki, M. Cytokinesis in animal cells. *Cold*  
524 *Spring Harbor perspectives in biology* **7**, a015834 (2015).
- 525 9. Glotzer, M. Cytokinesis in Metazoa and Fungi. *Cold Spring Harbor perspectives in*  
526 *biology* **9** (2017).
- 527 10. Knoblich, J.A. Asymmetric cell division: recent developments and their implications  
528 for tumour biology. *Nat Rev Mol Cell Biol* **11**, 849-860 (2010).
- 529 11. Cabernard, C., Prehoda, K.E. & Doe, C.Q. A spindle-independent cleavage furrow  
530 positioning pathway. *Nature* **467**, 91-94 (2010).
- 531 12. Roth, M., Roubinet, C., Ifflander, N., Ferrand, A. & Cabernard, C. Asymmetrically  
532 dividing *Drosophila* neuroblasts utilize two spatially and temporally independent  
533 cytokinesis pathways. *Nat Commun* **6**, 6551 (2015).
- 534 13. Tsankova, A., Pham, T.T., Garcia, D.S., Otte, F. & Cabernard, C. Cell Polarity  
535 Regulates Biased Myosin Activity and Dynamics during Asymmetric Cell Division  
536 via *Drosophila* Rho Kinase and Protein Kinase N. *Dev Cell* **42**, 143-155 e145 (2017).
- 537 14. Gallaud, E. *et al.* Ensconsin/Map7 promotes microtubule growth and centrosome  
538 separation in *Drosophila* neural stem cells. *J Cell Biol* **204**, 1111-1121 (2014).
- 539 15. Metivier, M. *et al.* Dual control of Kinesin-1 recruitment to microtubules by  
540 Ensconsin in *Drosophila* neuroblasts and oocytes. *Development* **146** (2019).
- 541 16. Widmann, T.J. & Dahmann, C. Dpp signaling promotes the cuboidal-to-columnar  
542 shape transition of *Drosophila* wing disc epithelia by regulating Rho1. *J Cell Sci* **122**,  
543 1362-1373 (2009).
- 544 17. Bischof, J. *et al.* A versatile platform for creating a comprehensive UAS-ORFeome  
545 library in *Drosophila*. *Development* **140**, 2434-2442 (2013).
- 546 18. Dietzl, G. *et al.* A genome-wide transgenic RNAi library for conditional gene  
547 inactivation in *Drosophila*. *Nature* **448**, 151-156 (2007).
- 548 19. Royou, A., Field, C., Sisson, J.C., Sullivan, W. & Karess, R. Reassessing the role and  
549 dynamics of nonmuscle myosin II during furrow formation in early *Drosophila*  
550 embryos. *Mol Biol Cell* **15**, 838-850 (2004).
- 551 20. Inoue, Y.H. *et al.* Mutations in orbit/mast reveal that the central spindle is comprised  
552 of two microtubule populations, those that initiate cleavage and those that propagate  
553 furrow ingression. *J Cell Biol* **166**, 49-60 (2004).

- 554 21. Minestrini, G., Harley, A.S. & Glover, D.M. Localization of Pavarotti-KLP in living  
555 *Drosophila* embryos suggests roles in reorganizing the cortical cytoskeleton during the  
556 mitotic cycle. *Mol Biol Cell* **14**, 4028-4038 (2003).
- 557 22. Adams, R.R., Tavares, A.A., Salzberg, A., Bellen, H.J. & Glover, D.M. pavarotti  
558 encodes a kinesin-like protein required to organize the central spindle and contractile  
559 ring for cytokinesis. *Genes Dev* **12**, 1483-1494 (1998).
- 560 23. Mathieu, J. *et al.* Aurora B and cyclin B have opposite effects on the timing of  
561 cytokinesis abscission in *Drosophila* germ cells and in vertebrate somatic cells. *Dev*  
562 *Cell* **26**, 250-265 (2013).
- 563 24. Claret, S., Jouette, J., Benoit, B., Legent, K. & Guichet, A. PI(4,5)P<sub>2</sub> produced by the  
564 PI4P5K SKTL controls apical size by tethering PAR-3 in *Drosophila* epithelial cells.  
565 *Curr Biol* **24**, 1071-1079 (2014).
- 566 25. Gervais, L., Claret, S., Januschke, J., Roth, S. & Guichet, A. PIP5K-dependent  
567 production of PIP<sub>2</sub> sustains microtubule organization to establish polarized transport  
568 in the *Drosophila* oocyte. *Development* **135**, 3829-3838 (2008).
- 569 26. Caous, R. *et al.* Spindle assembly checkpoint inactivation fails to suppress neuroblast  
570 tumour formation in aurA mutant *Drosophila*. *Nat Commun* **6**, 8879 (2015).
- 571 27. Wang, H., Brust-Mascher, I. & Scholey, J.M. The microtubule cross-linker Feo  
572 controls the midzone stability, motor composition, and elongation of the anaphase B  
573 spindle in *Drosophila* embryos. *Mol Biol Cell* **26**, 1452-1462 (2015).
- 574 28. Basto, R. *et al.* Flies without centrioles. *Cell* **125**, 1375-1386 (2006).
- 575 29. Hyman, A. *et al.* Preparation of modified tubulins. *Methods Enzymol* **196**, 478-485  
576 (1991).
- 577 30. Ramirez-Rios, S. *et al.* A TIRF microscopy assay to decode how tau regulates EB's  
578 tracking at microtubule ends. *Methods Cell Biol* **141**, 179-197 (2017).
- 579 31. Lee, M.J., Gergely, F., Jeffers, K., Peak-Chew, S.Y. & Raff, J.W. Msps/XMAP215  
580 interacts with the centrosomal protein D-TACC to regulate microtubule behaviour.  
581 *Nat Cell Biol* **3**, 643-649 (2001).
- 582 32. Goshima, G. & Vale, R.D. Cell cycle-dependent dynamics and regulation of mitotic  
583 kinesins in *Drosophila* S2 cells. *Mol Biol Cell* **16**, 3896-3907 (2005).
- 584 33. Rogers, S.L., Rogers, G.C., Sharp, D.J. & Vale, R.D. *Drosophila* EB1 is important for  
585 proper assembly, dynamics, and positioning of the mitotic spindle. *J Cell Biol* **158**,  
586 873-884 (2002).
- 587 34. Jordan, P. & Karess, R. Myosin light chain-activating phosphorylation sites are  
588 required for oogenesis in *Drosophila*. *J Cell Biol* **139**, 1805-1819 (1997).
- 589 35. Rueden, C.T. *et al.* ImageJ2: ImageJ for the next generation of scientific image data.  
590 *BMC bioinformatics* **18**, 529 (2017).
- 591 36. Roubinet, C. *et al.* Spatio-temporally separated cortical flows and spindle geometry  
592 establish physical asymmetry in fly neural stem cells. *Nat Commun* **8**, 1383 (2017).
- 593 37. Reber, S.B. *et al.* XMAP215 activity sets spindle length by controlling the total mass  
594 of spindle microtubules. *Nat Cell Biol* **15**, 1116-1122 (2013).
- 595 38. Cullen, C.F., Deak, P., Glover, D.M. & Ohkura, H. mini spindles: A gene encoding a  
596 conserved microtubule-associated protein required for the integrity of the mitotic  
597 spindle in *Drosophila*. *J Cell Biol* **146**, 1005-1018 (1999).
- 598 39. Fox, J.C., Howard, A.E., Currie, J.D., Rogers, S.L. & Slep, K.C. The XMAP215  
599 family drives microtubule polymerization using a structurally diverse TOG array. *Mol*  
600 *Biol Cell* **25**, 2375-2392 (2014).
- 601 40. Goshima, G., Wollman, R., Stuurman, N., Scholey, J.M. & Vale, R.D. Length control  
602 of the metaphase spindle. *Curr Biol* **15**, 1979-1988 (2005).

- 603 41. Edzuka, T. & Goshima, G. Drosophila kinesin-8 stabilizes the kinetochore-  
604 microtubule interaction. *J Cell Biol* **218**, 474-488 (2019).
- 605 42. Laycock, J.E., Savoian, M.S. & Glover, D.M. Antagonistic activities of Klp10A and  
606 Orbit regulate spindle length, bipolarity and function in vivo. *J Cell Sci* **119**, 2354-  
607 2361 (2006).
- 608 43. Morales-Mulia, S. & Scholey, J.M. Spindle Pole Organization in Drosophila S2 Cells  
609 by Dynein, Abnormal Spindle Protein (Asp), and KLP10A. *Mol Biol Cell* **16**, 3176-  
610 3186 (2005).
- 611 44. Radford, S.J., Harrison, A.M. & McKim, K.S. Microtubule-depolymerizing kinesin  
612 KLP10A restricts the length of the acentrosomal meiotic spindle in Drosophila  
613 females. *Genetics* **192**, 431-440 (2012).
- 614 45. Buster, D.W., Zhang, D. & Sharp, D.J. Poleward tubulin flux in spindles: regulation  
615 and function in mitotic cells. *Mol Biol Cell* **18**, 3094-3104 (2007).
- 616 46. Royou, A., Sullivan, W. & Karess, R. Cortical recruitment of nonmuscle myosin II in  
617 early syncytial Drosophila embryos: its role in nuclear axial expansion and its  
618 regulation by Cdc2 activity. *J Cell Biol* **158**, 127-137 (2002).
- 619 47. D'Avino, P.P., Savoian, M.S. & Glover, D.M. Cleavage furrow formation and  
620 ingression during animal cytokinesis: a microtubule legacy. *J Cell Sci* **118**, 1549-1558  
621 (2005).
- 622 48. Basant, A. *et al.* Aurora B kinase promotes cytokinesis by inducing centralspindlin  
623 oligomers that associate with the plasma membrane. *Dev Cell* **33**, 204-215 (2015).
- 624 49. Verni, F. *et al.* Feo, the Drosophila homolog of PRC1, is required for central-spindle  
625 formation and cytokinesis. *Curr Biol* **14**, 1569-1575 (2004).
- 626 50. Rusan, N.M. & Peifer, M. A role for a novel centrosome cycle in asymmetric cell  
627 division. *J Cell Biol* **177**, 13-20 (2007).
- 628 51. Januschke, J. & Gonzalez, C. Drosophila asymmetric division, polarity and cancer.  
629 *Oncogene* **27**, 6994-7002 (2008).
- 630 52. Rebollo, E. *et al.* Functionally unequal centrosomes drive spindle orientation in  
631 asymmetrically dividing Drosophila neural stem cells. *Dev Cell* **12**, 467-474 (2007).
- 632 53. Murthy, K. & Wadsworth, P. Dual role for microtubules in regulating cortical  
633 contractility during cytokinesis. *J Cell Sci* **121**, 2350-2359 (2008).
- 634 54. Strickland, L.I., Donnelly, E.J. & Burgess, D.R. Induction of cytokinesis is  
635 independent of precisely regulated microtubule dynamics. *Mol Biol Cell* **16**, 4485-  
636 4494 (2005).
- 637 55. Canman, J.C. *et al.* Determining the position of the cell division plane. *Nature* **424**,  
638 1074-1078 (2003).
- 639 56. Kotynkova, K., Su, K.C., West, S.C. & Petronczki, M. Plasma Membrane Association  
640 but Not Midzone Recruitment of RhoGEF ECT2 Is Essential for Cytokinesis. *Cell*  
641 *reports* **17**, 2672-2686 (2016).
- 642 57. Kaltschmidt, J.A., Davidson, C.M., Brown, N.H. & Brand, A.H. Rotation and  
643 asymmetry of the mitotic spindle direct asymmetric cell division in the developing  
644 central nervous system. *Nat Cell Biol* **2**, 7-12 (2000).
- 645 58. Adriaans, I.E., Basant, A., Ponsioen, B., Glotzer, M. & Lens, S.M.A. PLK1 plays dual  
646 roles in centralspindlin regulation during cytokinesis. *J Cell Biol* **218**, 1250-1264  
647 (2019).
- 648 59. Verma, V. & Maresca, T.J. Microtubule plus-ends act as physical signaling hubs to  
649 activate RhoA during cytokinesis. *eLife* **8** (2019).
- 650 60. Minestrini, G., Mathe, E. & Glover, D.M. Domains of the Pavarotti kinesin-like  
651 protein that direct its subcellular distribution: effects of mislocalisation on the tubulin  
652 and actin cytoskeleton during Drosophila oogenesis. *J Cell Sci* **115**, 725-736 (2002).

653  
654

## 655 Legend to the figures

656

### 657 Figure 1. Analysis of cell size asymmetry in *ensc* and Ensc-OE NBs

658 A) Scheme of a NB during cell division during metaphase (left) and telophase (right). Note  
659 that the NB cell division is asymmetric and produces a large NB and a small Ganglion Mother  
660 Cell (GMC) during cytokinesis. B) Selected images of a control NB (top) and an *ensc* mutant  
661 NB (bottom) during cell division. The membranes are displayed in green and the MTs are  
662 displayed in magenta. Time is min:s. Scale bar: 10 $\mu$ m. C) Dot plot showing the mitotic  
663 spindle length/NB diameter ratio ( $\pm$  s.d.) in control ( $0.86\pm 0.05$ ,  $n=27$ ) or in *ensc* NBs  
664 ( $0.79\pm 0.06$ ,  $n=23$ ), \*\*\*:  $P<0.0001$  (Wilcoxon test). D) Dot plot showing the NB  
665 diameter/GMC diameter ratio ( $\pm$  s.d.) in control ( $2.29\pm 0.20$ ,  $n=27$ ) or in *ensc* NBs ( $2.16\pm 0.20$ ,  
666  $n=23$ ), \*:  $P<0.05$  (Wilcoxon test). E) Kymographs showing microtubules assembled from  
667 GMPCPP seeds and 14  $\mu$ M tubulin in absence or in presence of 200 nM of MBP or MBP-  
668 Ensconsin. Horizontal and vertical scale bar are 5 $\mu$ m and 60s respectively. F) Graphs  
669 showing the growth and shrinkage rates and the catastrophe and rescue frequencies  
670 determined from kymographs shown in E. ns: non significant; \*\*\*\*:  $P<0.0001$  (Kruskal-  
671 Wallis ANOVA followed by post-hoc Dunn's multiple comparison, total number of growth  
672 events = 116, 123 and 107, shrinkage events = 67, 73 and 81, catastrophe events = 94, 96, 83  
673 and rescue events = 3, 3 and 33 for the control, MPB and MPB-ensconsin respectively). G)  
674 Selected images of a control NB (top) and an Ensc-OE NB (bottom) during cell division.  
675 Membranes are displayed in magenta and MTs or Ensconsin are displayed in green. H) Dot  
676 plot showing the mitotic spindle length/NB diameter ratio ( $\pm$  s.d.) in control ( $0.86\pm 0.06$ ,  
677  $n=25$ ) or in Ensc-OE NBs ( $0.95\pm 0.08$ ,  $n=19$ ), \*\*\*\*:  $P<0.0001$  (Wilcoxon test). I) Dot plot  
678 showing the NB diameter/GMC diameter ratio ( $\pm$  s.d.) in control ( $2.36\pm 0.17$ ,  $n=25$ ) or in  
679 Ensc-OE NBs ( $2.40\pm 0.19$ ,  $n=19$ ), ns: non-significant (Wilcoxon test) J) Summary of NB  
680 division in *ensc* (left) or Ensc-OE (right). *ensc* mutant NBs display shorter spindles and  
681 undergo less asymmetric cell division while Ensc-OE NBs, despite harboring long spindles,  
682 divides asymmetrically similar to WT. Time is min:s.

683

### 684 Figure 2. Analysis of cell size asymmetry in NB following modification of several MAP 685 protein levels



686 A) Selected images of control (top), Msps-OE (middle) and *Klp67A* RNAi (bottom) NBs. The  
687 membranes are shown in green, the MTs (top and bottom) and Msps (middle) are shown in  
688 magenta. Time is min:s. Scale bar: 10 $\mu$ m. B) Dot plot showing the mitotic spindle length/NB  
689 diameter ratio ( $\pm$  s.d.) in the NB of control ( $0.86\pm 0.06$ ,  $n=18$ ) or in Msps-OE transgenic flies  
690 ( $1.03\pm 0.1$ ,  $n=23$ ), \*\*\*\*:  $P<0.0001$  (Wilcoxon test). C) Dot plot showing the NB  
691 diameter/GMC diameter ratio ( $\pm$  s.d.) in control ( $2.34\pm 0.16$ ,  $n=18$ ) or in Msps-OE NBs  
692 ( $2.29\pm 0.28$ ,  $n=21$ ), ns: non-significant (Wilcoxon test). D) Dot plot showing the mitotic  
693 spindle length/NB diameter ratio ( $\pm$  s.d.) in control NBs ( $0.83\pm 0.07$ ,  $n=40$ ) or in *Klp67A*  
694 RNAi NBs ( $1.19\pm 0.15$ ,  $n=30$ ), \*\*\*\*:  $P<0.0001$  (Wilcoxon test). E) Dot plot showing the NB  
695 diameter/GMC diameter ratio in control ( $2.31\pm 0.16$ ,  $n=40$ ) or in *Klp67A* RNAi NBs  
696 ( $2.32\pm 0.23$ ,  $n=30$ ), ns: non-significant (Wilcoxon test). F) Selected images of control (top),  
697 *Klp10A*-OE (middle) and *Klp67A*-OE (bottom) NBs. The membranes are shown in green, the  
698 MTs are shown in magenta. Scale bar: 10 $\mu$ m. Time is min:s. G) Dot plot showing the mitotic  
699 spindle length/NB diameter ratio ( $\pm$  s.d.) in control NBs ( $0.79\pm 0.08$ ,  $n=49$ ) or in *Klp10A*-OE  
700 NBs ( $0.63\pm 0.09$ ,  $n=49$ ), \*\*\*\*:  $P<0.0001$  (Wilcoxon test). H) Dot plot showing the NB  
701 diameter/GMC diameter ratio ( $\pm$  s.d.) in control NBs ( $2.29\pm 0.17$ ,  $n=49$ ) or in *Klp10A*-OE  
702 NBs ( $2.00\pm 0.27$ ,  $n=49$ ), \*\*\*\*:  $P<0.0001$  (Wilcoxon test). I) Dot plot showing the mitotic  
703 spindle length/NB diameter in control NBs ( $0.83\pm 0.07$ ,  $n=40$ ) or in *Klp67A*-OE NBs  
704 ( $0.73\pm 0.08$ ,  $n=48$ ), \*\*\*\*:  $P<0.0001$  (Wilcoxon test). J) Dot plot showing the NB  
705 diameter/GMC diameter ratio in control NBs ( $2.32\pm 0.16$ ,  $n=40$ ) or in *Klp67A* RNAi NBs  
706 ( $2.19\pm 0.18$ ,  $n=48$ ), \*\*\*\*:  $P<0.0001$  (Wilcoxon test).

707

708 **Figure 3. Analysis of myosin dynamics and furrow positioning in *ensc*, *Klp67*-OE and**  
709 ***Klp10A*-OE**

710 A) Selected images of (from top to bottom) dividing control, *ensc*, *Klp67A*-OE and *Klp10A*-  
711 OE NBs expressing tubulin (magenta) and myosin regulatory light chain (green and lower  
712 panels in monochrome) after anaphase onset ( $t=20s$ ) till late telophase. Scale bar: 10 $\mu$ m. Time  
713 is s. B) Scheme showing the possible apical shift between the initial and final furrow  
714 curvature analysis. C) Dot plot showing of the relative furrow displacement between early  
715 anaphase and late telophase in control ( $0.00\pm 0.04$ ,  $n=18$ ), *ensc* ( $-0.03\pm 0.05$ ,  $n=18$ ), *Klp67A*-  
716 OE ( $-0.05\pm 0.04$ ,  $n=12$ ), and *Klp10A*-OE NBs ( $-0.14\pm 0.04$ ,  $n=22$ ). \*:  $P<0.05$ , \*\*:  $P<0.001$ ,  
717 \*\*\*\*:  $P<0.0001$  (Wilcoxon test). D) Scheme showing the furrow width (red) during mid  
718 anaphase. E) Dot plot showing the relative myosin furrow width/cell length ratio for control

719 (0.08±0.02,  $n=18$ ), *ensc* (0.14±0.07,  $n=17$ ), Klp67A-OE (0.13±0.05,  $n=12$ ), and Klp10A-OE  
720 NBs (0.25±0.11,  $n=23$ ), \*:  $P<0.05$ , \*\*\*:  $P<0.001$ , \*\*\*\*:  $P<0.0001$  (Wilcoxon test)).

721

722 **Figure 4. Analysis of centralspindlin localization and dynamics in control, *ensc*, Klp10A-  
723 OE and *sas-4<sup>s2214</sup>* NBs**

724 A) Selected images of dividing control expressing tubulin (magenta) and GFP-Pav-klp (green  
725 and lower panels in monochrome) from anaphase onset till late telophase (top left). B) *ensc*  
726 NB. C) Klp10A-OE NB. D) *sas-4<sup>s2214</sup>* NBs (bottom). Scale bar: 10µm. Time is s. E) Higher  
727 magnification view of the selected control *ensc*, Klp10A-OE and *sas-4<sup>s2214</sup>* telophase NBs  
728 (from panels in A-D) showing GFP-Pav-klp localization at the cleavage site. See the strong  
729 signal at the cell cortex (red arrowheads) and the weak signal at the presumptive spindle  
730 midzone away from the cleavage site, toward the apical side blue (blue arrows). F) Scheme of  
731 the cleavage site showing the cortical and midzone centralspindlin pools. G) Dot plot (± s.d.)  
732 showing the relative cortical/midzone GFP intensity ratio for control (2.57±1.13,  $n=15$ ), *ensc*  
733 (1.75±0.52,  $n=11$ ), Klp10A-OE (1.20±0.53,  $n=12$ ), *sas-4<sup>s2214</sup>* (1.24±0.54,  $n=10$ ), control  
734 (4.2±1.76,  $n=7$ ) and Klp67A-OE NBs (2.17±1.15,  $n=11$ ). \*:  $P<0.05$ , \*\*\*:  $P<0.001$ , \*\*\*\*:  
735  $P<0.0001$  (Wilcoxon test).

736

737 **Figure 5. Analysis of the spindle midzone and the cleavage furrow position in brain NBs  
738 during cell division**

739 A) Selected images of a WT NB expressing Feo-GFP (green and lower panels in  
740 monochrome), MTs (magenta), and membranes during cell division (green and lower panels  
741 in monochrome). The metaphase plate is indicated by a white arrowhead (-120s). The spindle  
742 midzone is indicated by red arrowheads and the furrow is indicated by green arrowheads (60-  
743 300s). Scale bar: 10 µm. Time is s. B) Kymograph showing the localization of the spindle  
744 midzone and the cell contours during the time course of the NB cell division shown in panel  
745 A, along the apico-basal axis. C) Dot Plot (± s.d.) showing the mean relative metaphase plate  
746 position along the apico-basal cortex 90 sec after anaphase onset (0.56± 0.02  $n=21$ ). D) Dot  
747 Plot showing the mean relative spindle midzone position (± s.d.) along the apico-basal cortex  
748 90 sec after anaphase onset (0.59±0.02,  $n=23$ ). E) Dot Plot (± s.d.) showing the mean relative  
749 furrow position along the apico-basal cortex 90 sec after anaphase onset (0.72±0.13,  $n=23$ ). F)  
750 Dot Plot (± s.d.) showing the mean relative distance between the furrow position and the  
751 spindle midzone 90 sec after anaphase onset (0.13 ± 0.02,  $n=23$ ).

752

753 **Figure S1. Western Blot analyses of Enscosin, Minispindles, Klp10A, Klp67A protein**  
754 **in brain extracts**

755 Brain subjected to RNAi or overexpression (OE) for the indicated MAPs were dissected and  
756 resuspended in sample buffer before for Western blot analyses. The primary antibody used for  
757 each Western blot is indicated at the bottom of each top panel. In the bottom panels, actin was  
758 used as a loading control.

759  
760

761 **Figure S2. Polarity-dependent apical myosin clearing and localization of aPKC and**  
762 **Miranda in *ensc*, Klp10A-OE and Klp67A-OE NBs**

763 A) Scheme of Myosin clearing from the apical cortex of neuroblast at metaphase/anaphase  
764 transition (left). Histogram showing the timing of apical myosin clearing (right) for NBs of  
765 the indicated genotypes in control ( $30.00 \pm 10.29$  s,  $n=18$ ), *ensc* ( $34.29 \pm 12.87$  s,  $n=21$ ),  
766 Klp67A-OE ( $28.57 \pm 12.92$  s,  $n=14$ ), Klp10A-OE ( $26.67 \pm 9.63$  s,  $n=24$ ) NBs. Time 0s is  
767 anaphase onset. ns: non-significant. (Wilcoxon test) B) Analysis of aPKC and Miranda  
768 localizations in control, Klp10A-OE, Klp67A-OE and in *ensc* metaphase NBs. Brains of the  
769 indicated genotypes were fixed and stained for aPKC (blue), Miranda (green),  $\alpha$ -tubulin (red)  
770 and phospho-histone H3 (Blue). Scale bar: 10 $\mu$ m. The number of examined cells (n) is also  
771 indicated. None of the conditions used compromise the location of aPKC and Miranda. C)  
772 Dot plot showing the NB diameter/GMC diameter ratio ( $\pm$  s.d.) in control ( $2.31 \pm 0.20$ ,  $n=12$ ),  
773 in *pav*<sup>B200/+</sup> ( $2.32 \pm 0.19$ ,  $n=20$ ), in *svn*<sup>2180/+</sup> ( $2.25 \pm 0.11$ ,  $n=16$ ), in Klp10A-OE ( $1.93 \pm 0.24$ ,  
774  $n=23$ ), in *pav*<sup>B200/+</sup>; Klp10A-OE ( $1.73 \pm 0.24$ ,  $n=21$ ), and in *svn*<sup>2180/+</sup>; Klp10A-OE ( $1.67 \pm 0.27$ ,  
775  $n=16$ ) NBs. ns: non-significant, \*\*:  $P < 0.01$ , \*\*\*\*:  $P < 0.0001$  (Wilcoxon test). Cell size  
776 asymmetry in Klp10A-OE NBs is enhanced by alteration of the CPC and the centralspindlin  
777 complex.

778  
779

780 **Figure S3. Midzone and cortical centralspindlin recruitment in control and colchicine-**  
781 **treated NBs**

782 A) Mean relative cortical/furrow (red) and central spindle (blue) enrichment of Pav-klp-GFP  
783 ( $\pm$  s.d.) in a control NB (regarding Figure 4 A). Pav-klp-GFP is rapidly recruited at the cortex  
784 while its recruitment at the centralspindle is slower.  $n=15$ . B) GFP-Pav-klp (green and lower  
785 panels in monochrome) is strongly recruited to the cell cortex and to the cleavage furrow in  
786 Mad2-depleted cells. In the absence of MTs (*Mad2* RNAi+colchicine), GFP-Pav-klp is faintly



787 detected at the basal cortex but is not enriched similarly to conditions where the MT  
788 cytoskeleton  
789 n is intact. Scale bar: 10 $\mu$ m. Time is s. C) Mean relative GFP-pav-Klp signal ( $\pm$  s.d.) at the  
790 cell cortex in *Mad2* RNAi with ( $n=9$ ) (grey) or without ( $n=7$ ) (dark grey) MTs.

791

792 **Figure S4. Analysis of centralspindlin levels at the centralspindle or the cleavage furrow**  
793 **during anaphase**

794 A) Dot plot showing the mean relative GFP-Pav-klp signal at the cleavage furrow 180 sec  
795 after anaphase onset in control ( $0.53\pm 0.17$ ,  $n=15$ ), *ensc* ( $0.34\pm 0.09$ ,  $n=11$ ) Klp10A-OE  
796 ( $0.36\pm 0.16$ ,  $n=12$ ), and *sas4<sup>s2214</sup>* ( $0.48\pm 0.27$ ,  $n=10$ ), control ( $0.32\pm 0.10$ ,  $n=7$ ), and Klp67A-  
797 OE ( $0.18\pm 0.05$ ,  $n=11$ ) NBs. ns: non-significant, \*\*\*\*\*:  $P<0.0001$ , (Student test and Wilcoxon  
798 test fort Klp67A-OE). B) Dot plot showing the total relative GFP-Pav-klp signal at the  
799 midzone 180 sec after anaphase onset in control ( $0.22\pm 0.07$ ,  $n=15$ ), *ensc* ( $0.224\pm 0.09$ ,  $n=11$ )  
800 Klp10A-OE ( $0.46\pm 0.20$ ,  $n=12$ ), and *sas4<sup>s2214</sup>* ( $0.38\pm 0.13$ ,  $n=10$ ), control ( $0.08\pm 0.04$ ,  $n=7$ ),  
801 and Klp67A-OE ( $0.12\pm 0.05$ ,  $n=11$ ) NBs. ns: non-significant, \*:  $P<0.05$ , \*\*:  $P<0.01$ , \*\*\*\*\*:  
802  $P<0.0001$ , (Student test and Wilcoxon test for Klp67A-OE).

803

804 **Figure S5. Analysis of centrosome contribution for cleavage positioning and of**  
805 **peripheral MTs in different backgrounds**

806 A) Dot plot showing the mitotic spindle length/NB diameter ratio ( $\pm$  s.d.) in control  
807 ( $0.85\pm 0.03$ ,  $n=12$ ) or *sas4<sup>s2214</sup>* NBs ( $1.32\pm 0.17$ ,  $n=17$ ), \*\*\*\*\*:  $P<0.0001$ , (Wilcoxon test) B)  
808 Dot plot showing the NB diameter/GMC diameter ratio ( $\pm$  s.d.) in control ( $2.31\pm 0.2$ ,  $n=12$ ) or  
809 *sas4<sup>s2214</sup>* NBs ( $1.94\pm 0.37$ ,  $n=19$ ). \*\*:  $P<0.01$  (Wilcoxon test). C) Selected images of control  
810 NBs (top) or NBs in which the basal centrosome has been laser-ablated (bottom). The green  
811 triangle shows the basal centrosome before ablation, the red triangle shows the position of the  
812 ablated centrosome. The NBs expressed GFP-H2A (to confirm the metaphase stage, anaphase  
813 onset and the position of the basal GMC), PH-PLC $\delta$ -GFP (to visualize cell contours) and  
814 GFP-Aurora A (to target the centrosomes). D) Dot plot showing the NB diameter/GMC  
815 diameter ratio ( $\pm$  s.d.) in control ( $2.29\pm 0.21$ ,  $n=9$ ) or basal centrosome-ablated NBs  
816 ( $1.98\pm 0.29$ ,  $n=12$ ). \*\*\*:  $P<0.001$ , (Student test). Scale bar: 10 $\mu$ m. Time is min:s. E) Selected  
817 high-resolution images of control, *ensc*, Klp67A-OE, and Klp10A-OE NBs. Tubulin is shown  
818 in red (and lower panels in monochrome), Myosin is shown in green, and phospho-Histone  
819 H3 (Ser10) in blue. The white ellipses show the peripheral MT bundles in the vicinity of the  
820 furrow. Scale bar: 10 $\mu$ m. F) Histogram showing the number of peripheral astral MTs bundles

821 detected at the vicinity of the middle cleavage plane in a Z series projection (1  $\mu\text{m}$ ) in control  
822 ( $2.3\pm 0.5$ ,  $n=9$ ), *ensc* ( $1.63\pm 0.52$ ,  $n=8$ ), Klp67A-OE ( $1.7\pm 0.48$ ,  $n=10$ ) and in Klp10A-OE  
823 ( $0.86\pm 0.69$ ,  $n=7$ ) NBs. \*:  $P<0.05$ , \*\*\*:  $P<0.001$  (Wilcoxon test).

824

#### 825 **Video 1. Asymmetric cell division in a control NB**

826 Microtubules (RFP- $\alpha$ -tubulin) are displayed in magenta and PH-PLC $\delta$ -GFP is displayed  
827 in green. Scale bar: 10  $\mu\text{m}$ . Time is min: s.

828

#### 829 **Video 2. Asymmetric cell division in a Msps-OE NB**

830 Microtubules (Msps-RFP) are displayed in magenta and PH-PLC $\delta$ -GFP is displayed in  
831 green. Scale bar: 10  $\mu\text{m}$ . Time is min: s.

832

#### 833 **Video 3. Asymmetric cell division in a Klp10A-OE NB**

834 Microtubules (RFP- $\alpha$ -tubulin) are displayed in red and PH-PLC $\delta$ -GFP is displayed in  
835 green. Scale bar: 10  $\mu\text{m}$ . Time is min: s.

836

#### 837 **Video 4. Cortical myosin dynamics during cytokinesis in a control NB**

838 Microtubules (mCherry- $\alpha$ -tubulin) are displayed in magenta and Sqh-GFP is displayed in  
839 green or monochrome (right). Scale bar: 10  $\mu\text{m}$ . Time is min: s.

840

#### 841 **Video 5. Cortical myosin dynamics during cytokinesis in an *ensc* NB**

842 Microtubules (mCherry- $\alpha$ -tubulin) are displayed in magenta and Sqh-GFP is displayed  
843 in green or monochrome (right). Scale bar: 10  $\mu\text{m}$ . Time is min: s.

844

#### 845 **Video 6. Cortical myosin dynamics during cytokinesis in a Klp10A-OE NB**

846 Microtubules (mCherry- $\alpha$ -tubulin) are displayed in magenta and Sqh-GFP is displayed in  
847 green or monochrome (right). Scale bar: 10  $\mu\text{m}$ . Time is min: s.

848

#### 849 **Video 7. Pavarotti-klp localization during cytokinesis in a control NB**

850 Microtubules (mCherry- $\alpha$ -tubulin) are displayed in magenta and GFP-Pav-klp is  
851 displayed in green or monochrome (right). Scale bar: 10  $\mu\text{m}$ . Time is min: s.

852

#### 853 **Video 8. Pavarotti-klp localization during cytokinesis in an *ensc* NB**

854 Microtubules (mCherry- $\alpha$ -tubulin) are displayed in magenta and GFP-Pav-klp is  
855 displayed in green or monochrome (right). Scale bar: 10  $\mu$ m. Time is min: s.

856

857 **Video 9. Pavarotti-klp localization during cytokinesis in a Klp10A-OE NB**

858 Microtubules (mCherry- $\alpha$ -tubulin) are displayed in magenta and GFP-Pav-klp is  
859 displayed in green or monochrome (right). Scale bar: 10  $\mu$ m. Time is min: s.

860

861 **Video 10. Asymmetric cell division in a control NB or after basal centrosome**  
862 **ablation**

863 The left panel shows a control NB. The right panel shows a NB in which the basal  
864 centrosome was ablated. First and second images show pre and post ablation images  
865 respectively before acquisition. Aurora A-GFP, GFP-H2A and PH-PLC $\delta$ -GFP are displayed  
866 in grey. Scale bar: 10  $\mu$ m. Time is min: s.

867

868 **Video 11. Fascetto localization during cytokinesis in a control NB**

869 Microtubules (mCherry- $\alpha$ -tubulin) are displayed in magenta and PH-PLC $\delta$ -GFP and Feo-  
870 GFP are displayed in green or monochrome (right). Scale bar: 10  $\mu$ m. Time is min: s.

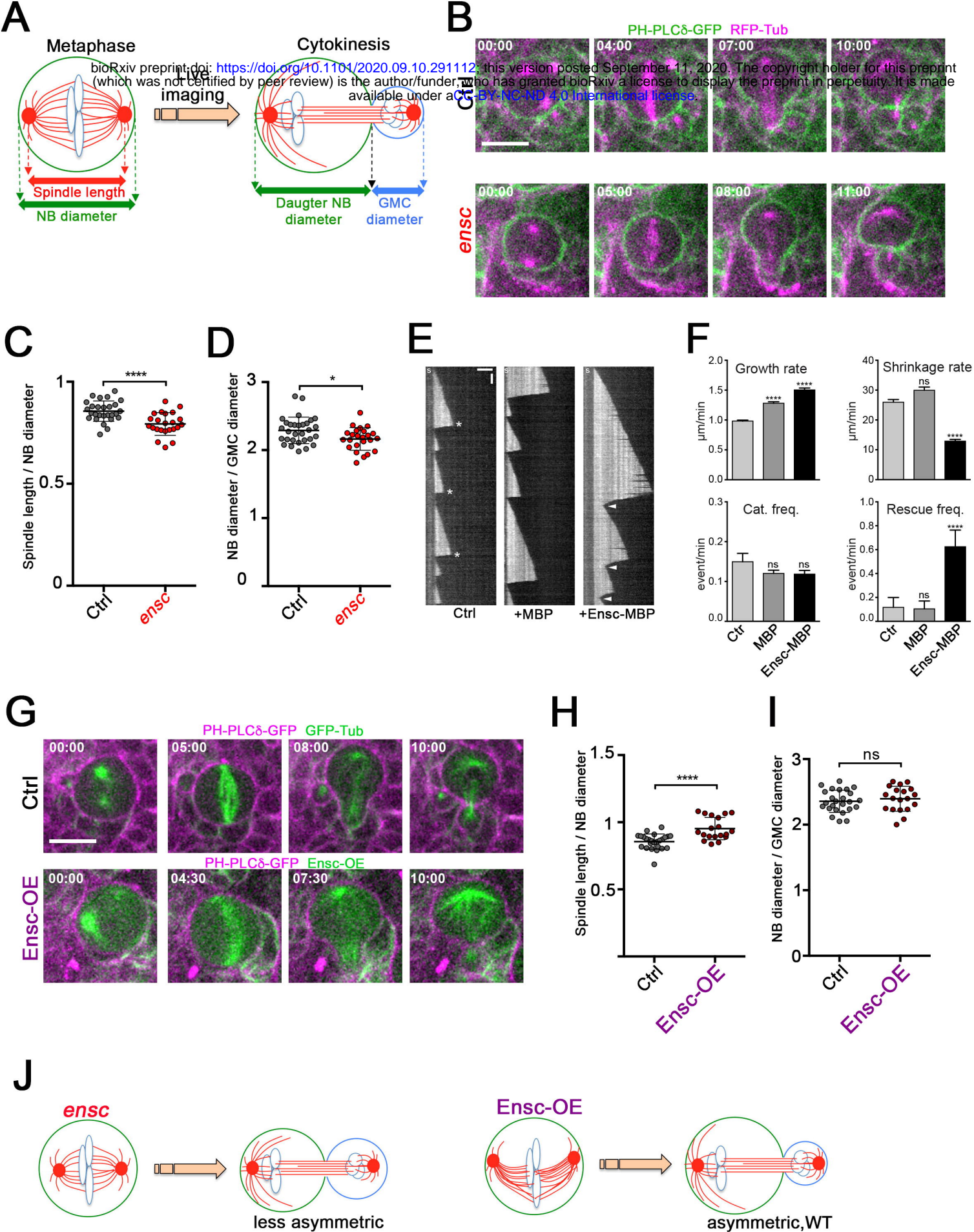
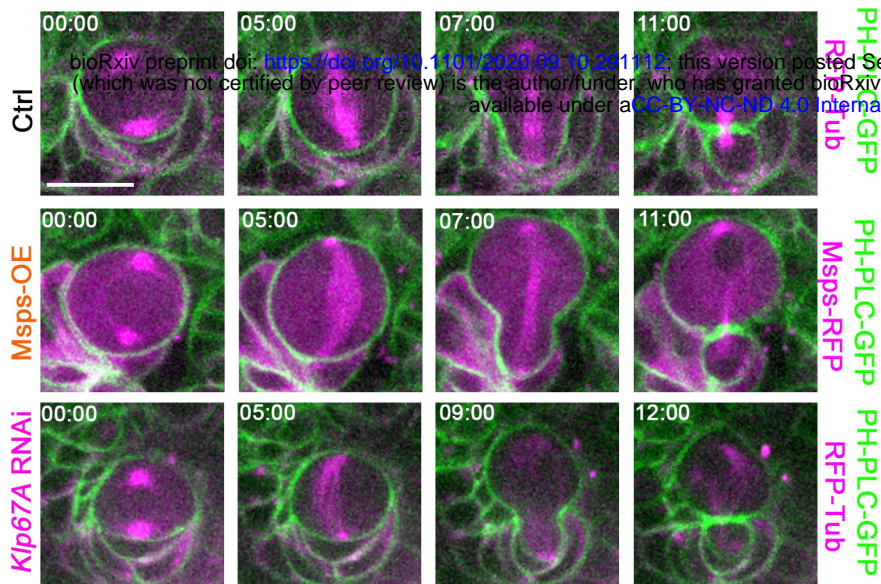
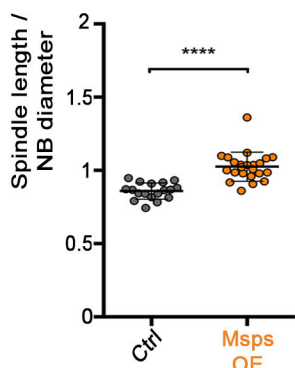
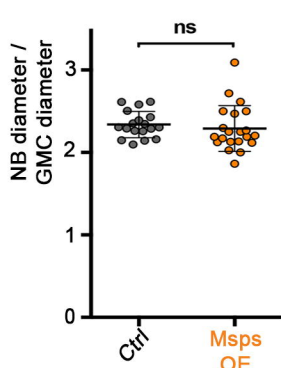
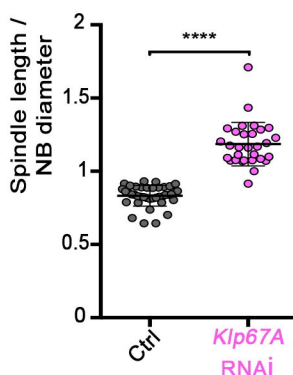
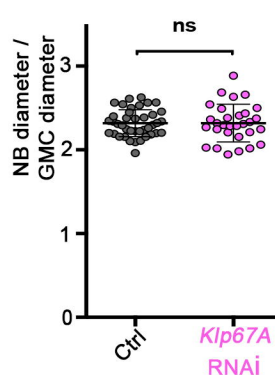
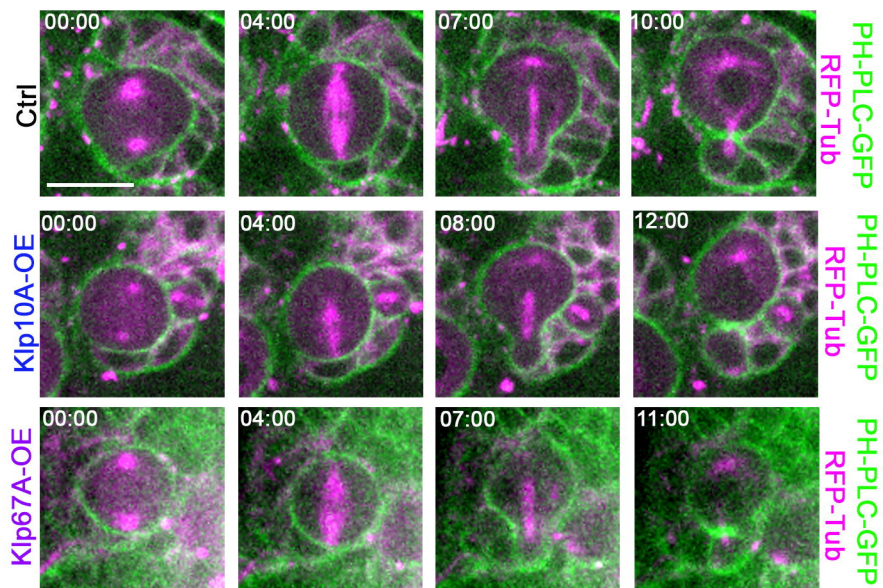
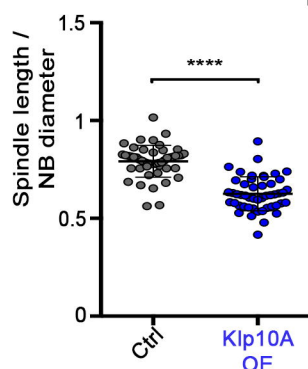
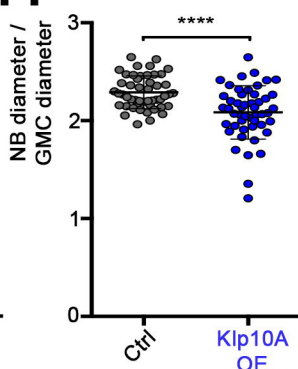
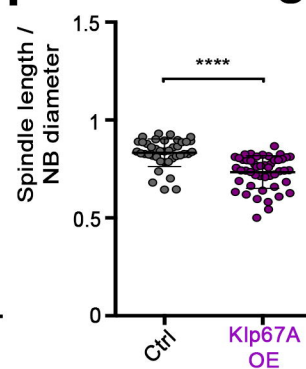
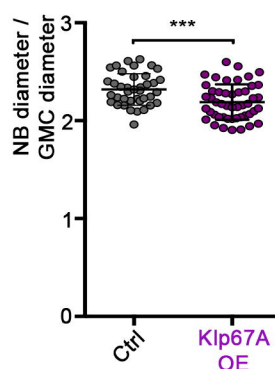


Figure 1



**A****B****C****D****E****F****G****H****I****J****Figure 2**



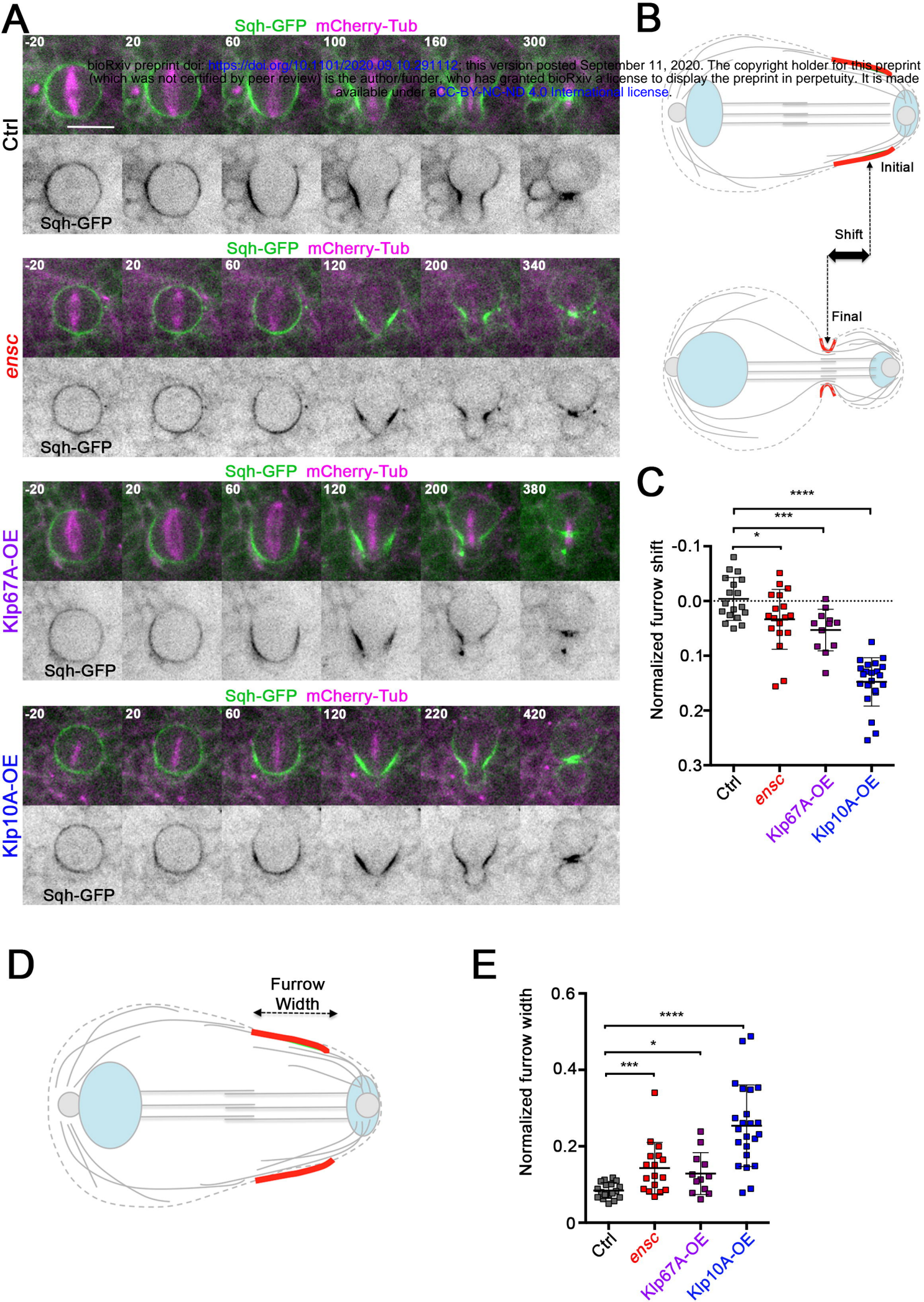


Figure 3



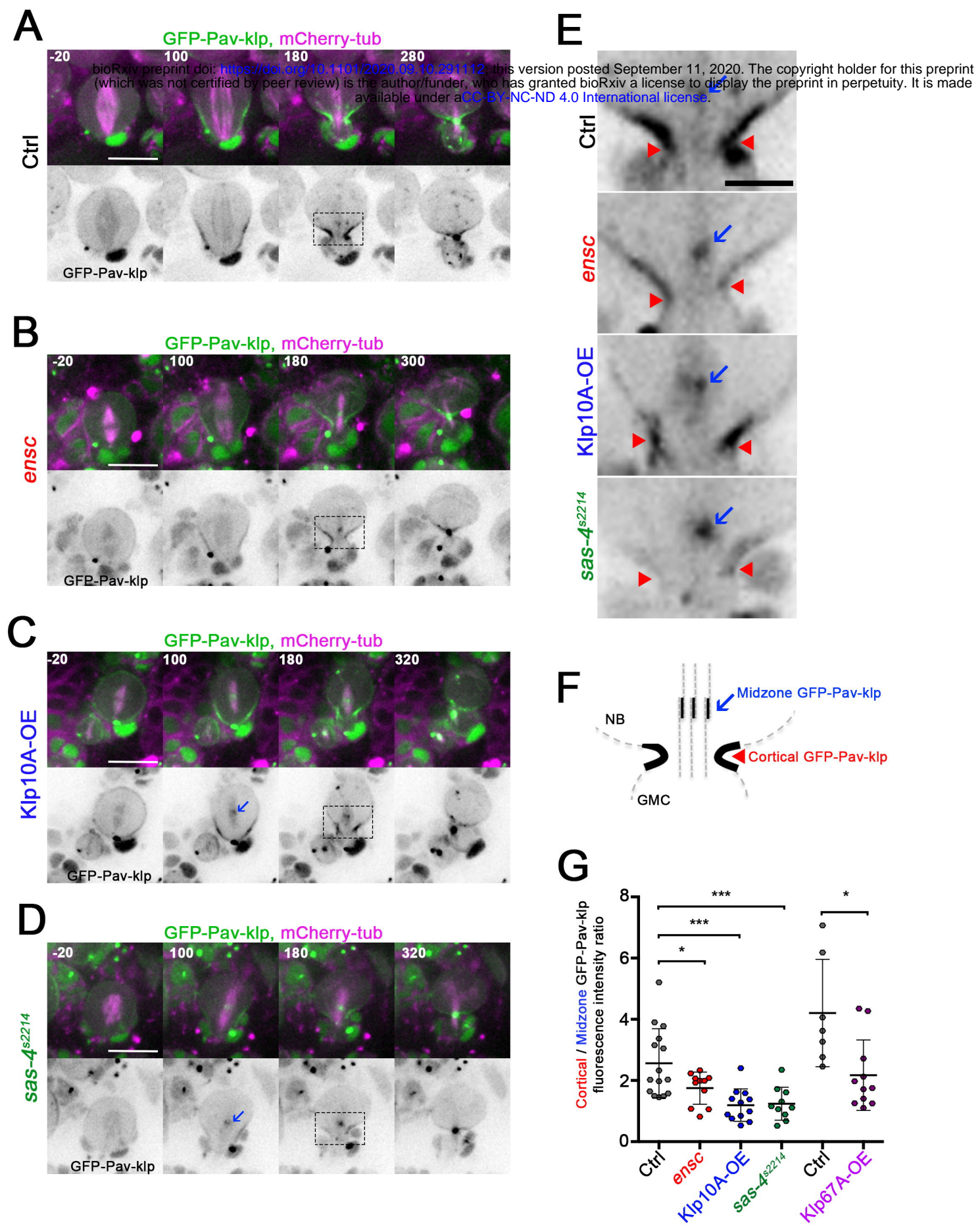


Figure 4

**A**

bioRxiv preprint doi: <https://doi.org/10.1101/2020.09.10.291112>; this version posted September 11, 2020. The copyright holder for this preprint (which was not certified by peer review) is the author/funder, who has granted bioRxiv a license to display the preprint in perpetuity. It is made available under aCC-BY-NC-ND 4.0 International license.

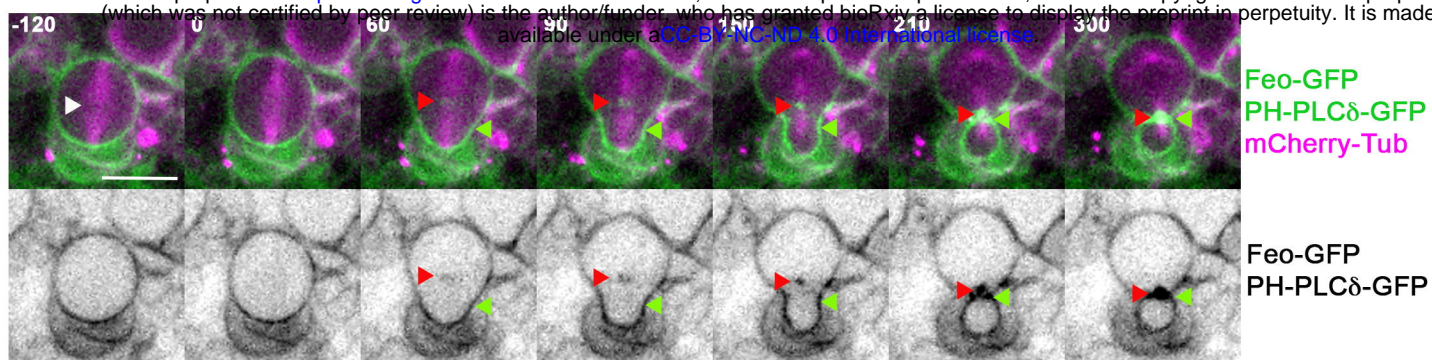
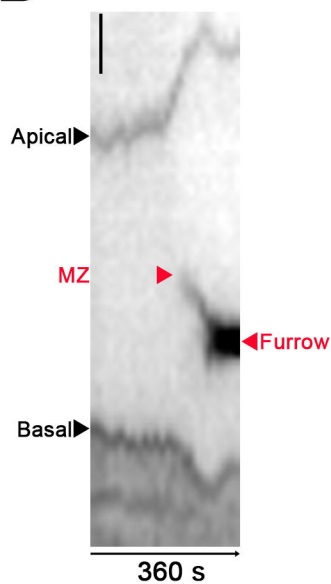
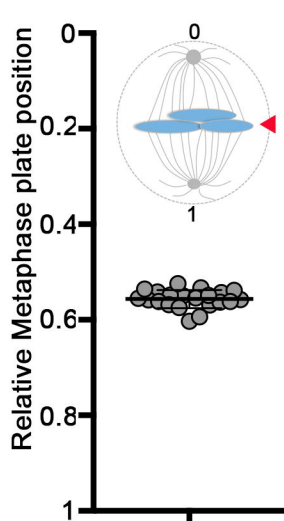
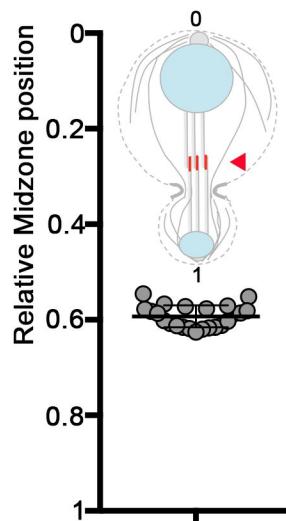
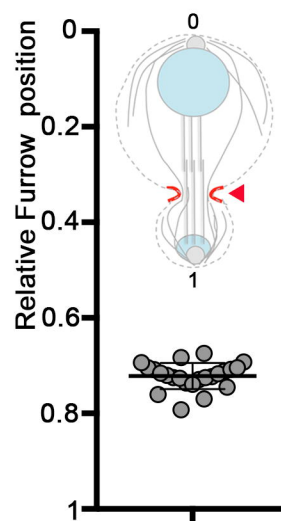
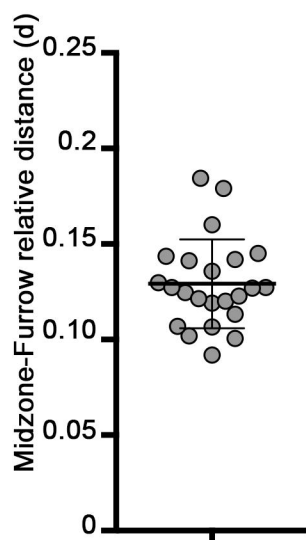
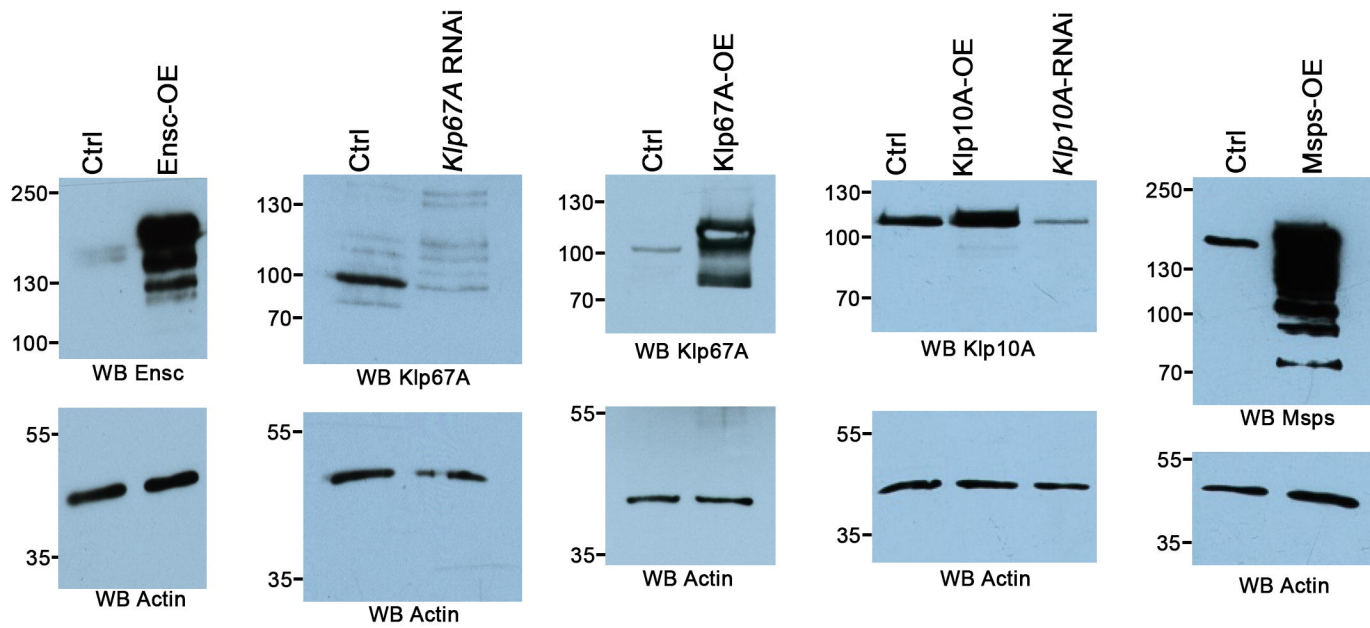
**B****C****D****E****F**

Figure 5

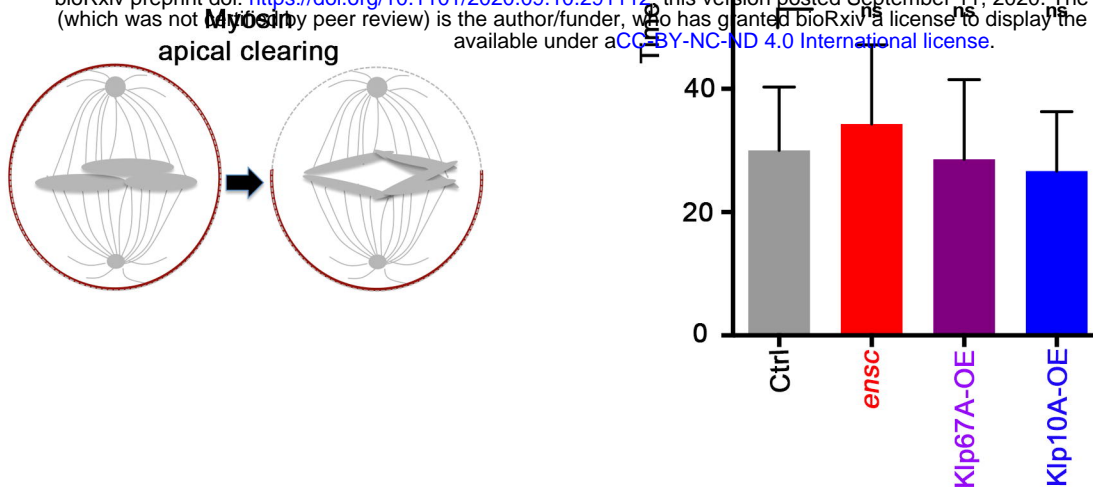




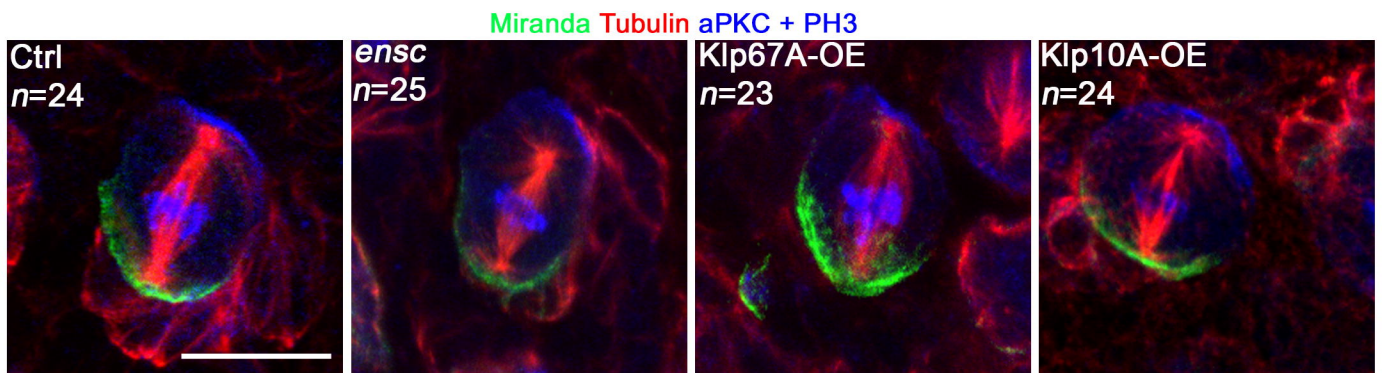
Supplementary Figure S1

A

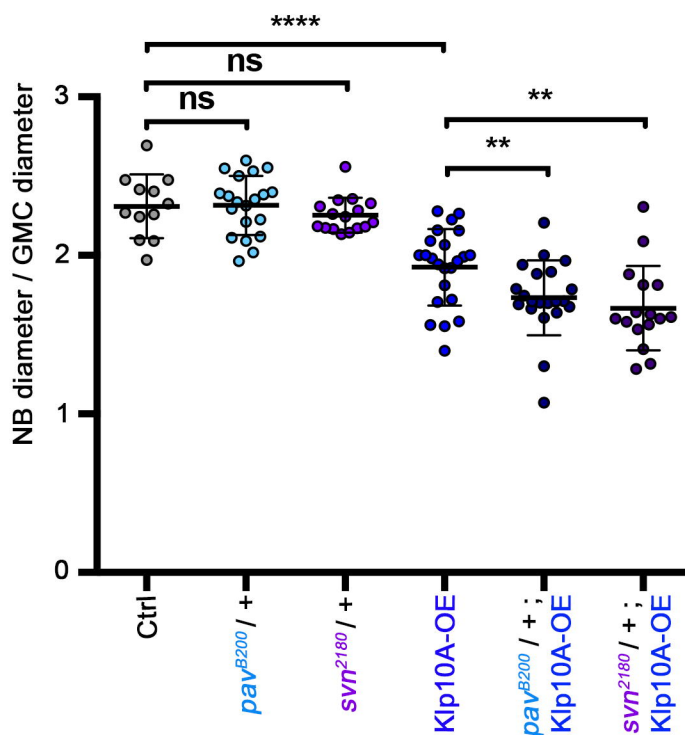
bioRxiv preprint doi: <https://doi.org/10.1101/2020.09.10.291117>; this version posted September 11, 2020. The copyright holder for this preprint (which was not certified by peer review) is the author/funder, who has granted bioRxiv a license to display the preprint in perpetuity. It is made available under aCC-BY-NC-ND 4.0 International license.



B

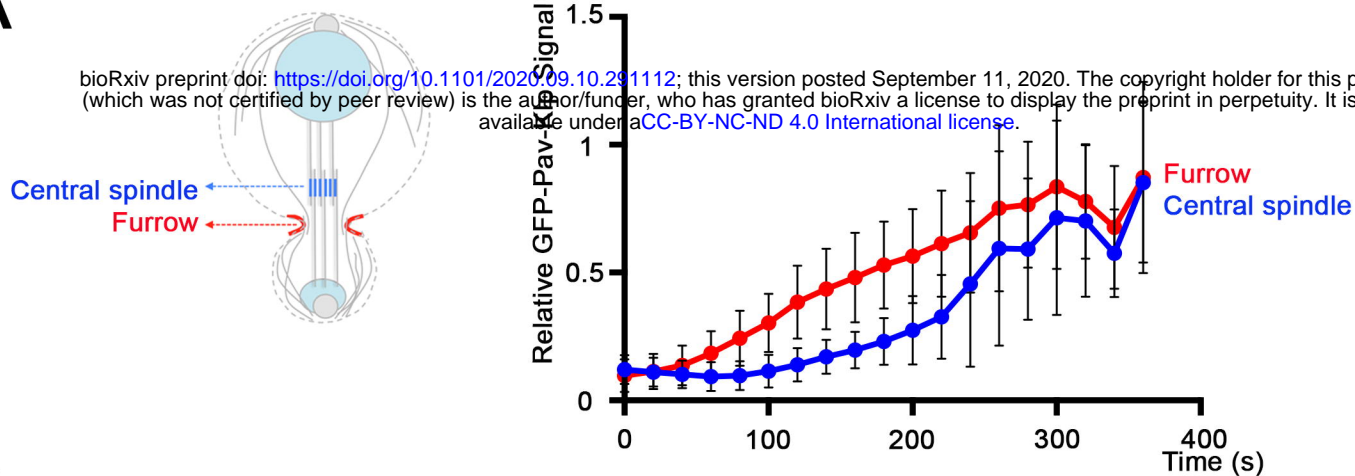


C

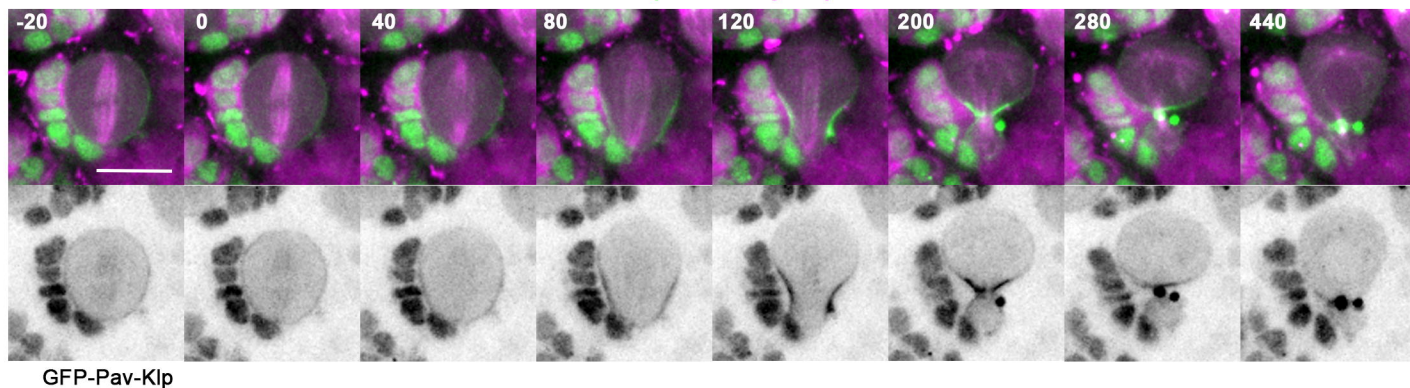


**A**

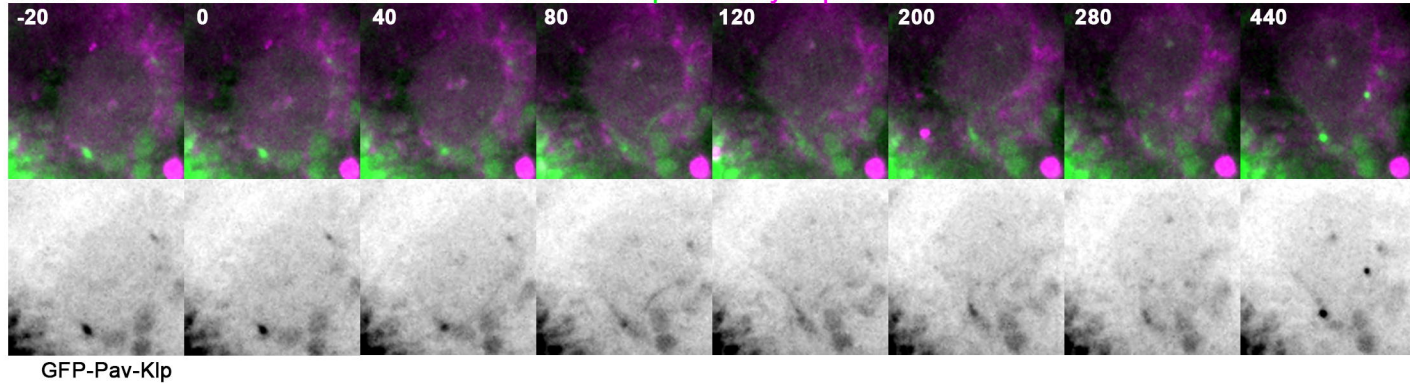
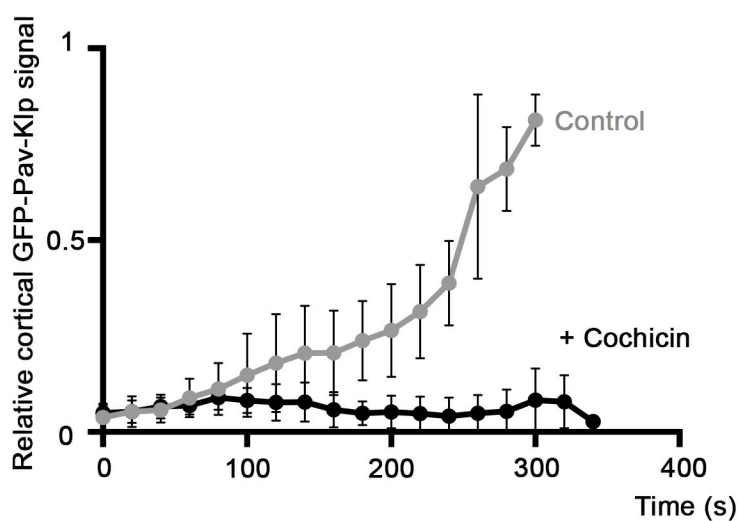
bioRxiv preprint doi: <https://doi.org/10.1101/2020.09.10.291112>; this version posted September 11, 2020. The copyright holder for this preprint (which was not certified by peer review) is the author/funder, who has granted bioRxiv a license to display the preprint in perpetuity. It is made available under aCC-BY-NC-ND 4.0 International license.

**B***Mad2* RNAi

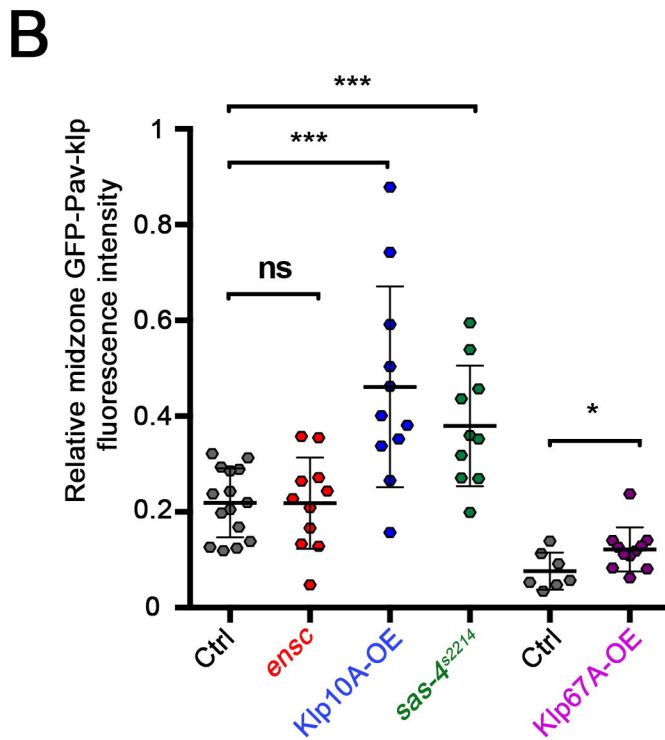
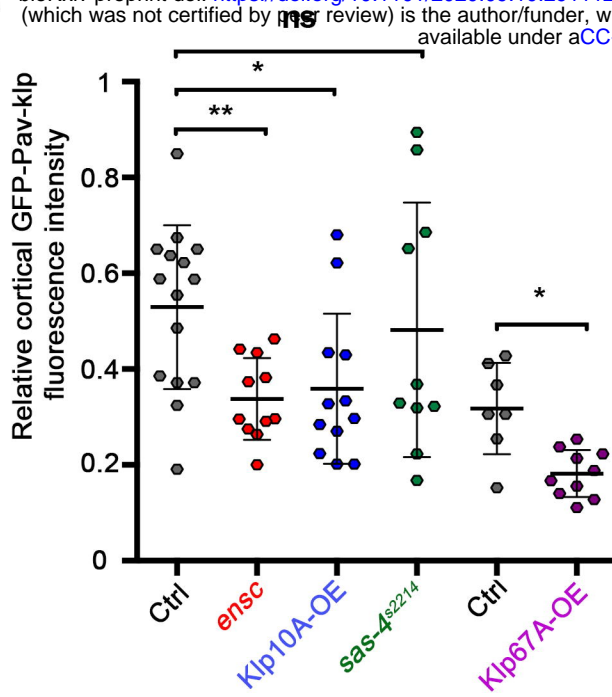
GFP-Pav-Klp mCherry-Jupiter

*Mad2* RNAi + colchicine

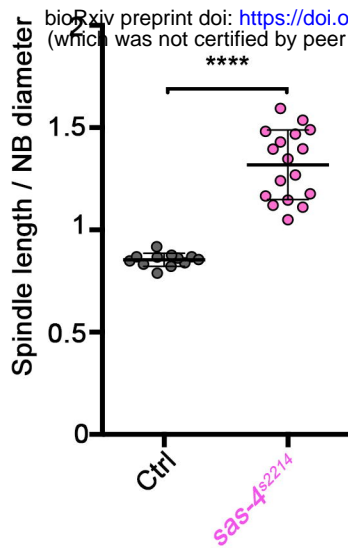
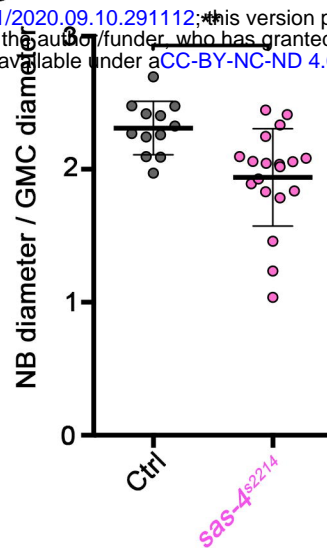
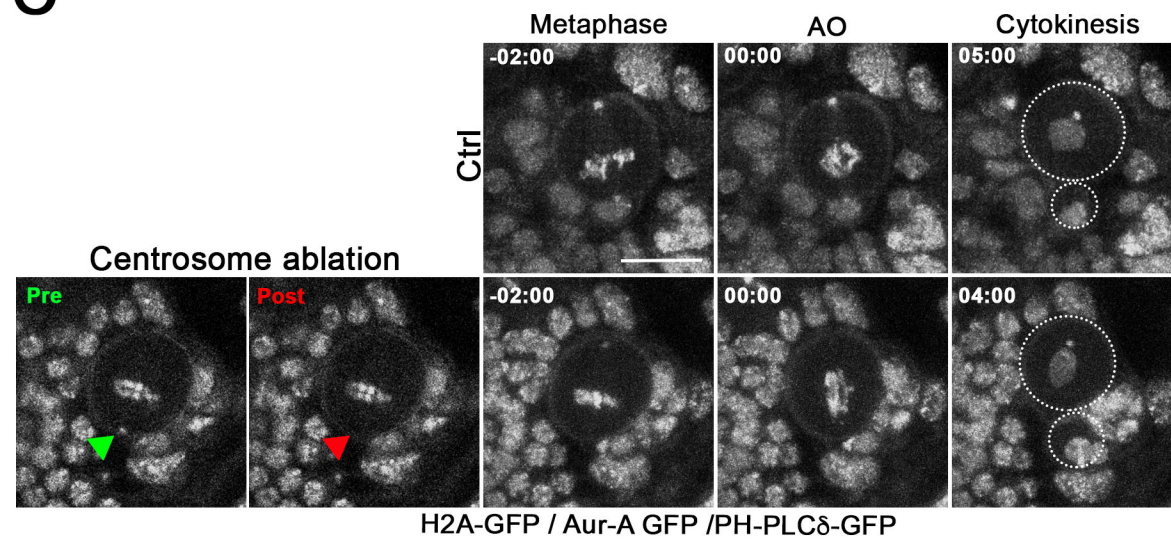
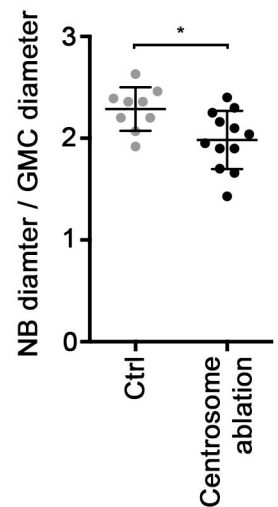
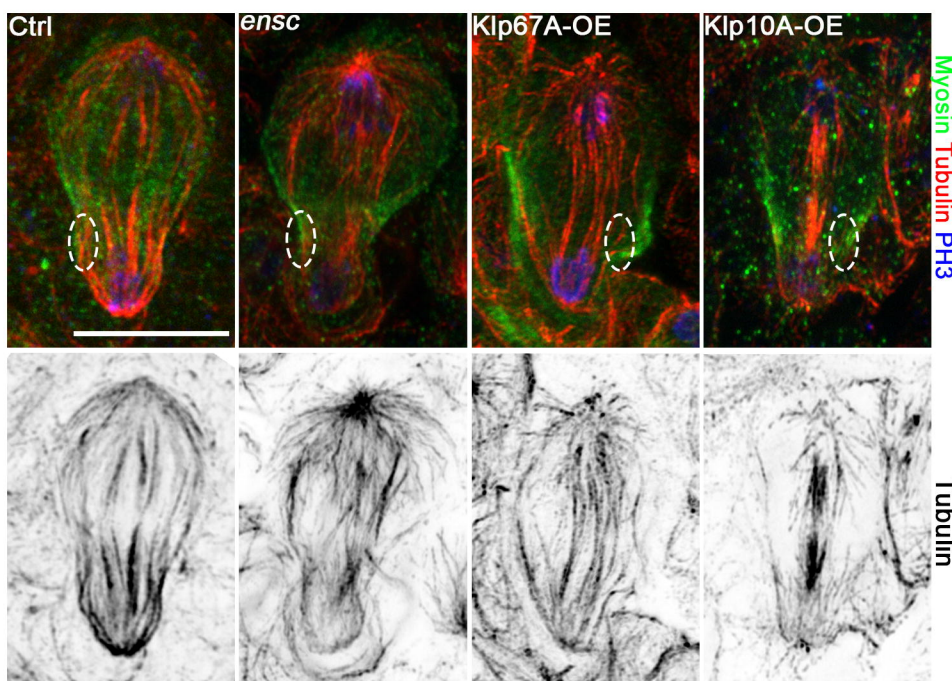
GFP-Pav-Klp mCherry-Jupiter

**C**

Supplementary Figure S3





**A****B****C****D****E****F**